DFT study of Functionalised Graphene as an Electrode Material for Sodium-Ion Batteries

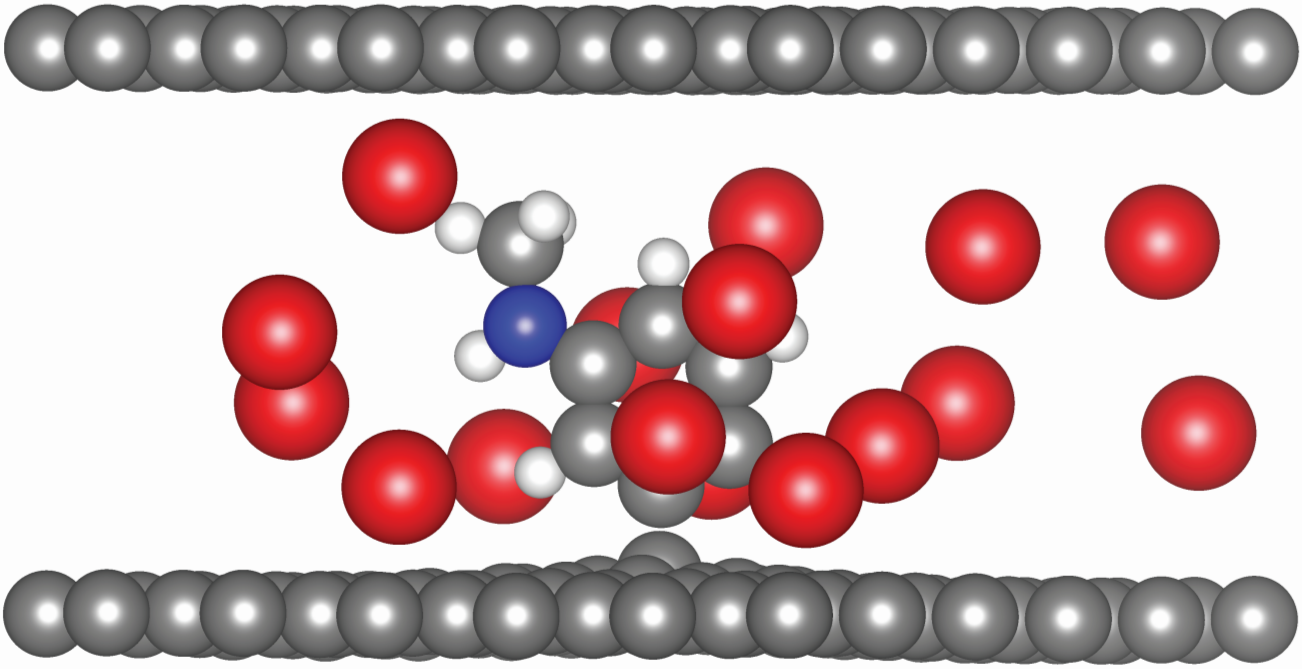

Testing the Viability of $NHCH_3$-Benzene, Aminobenzene and Phenol as Spacers Between Graphene Layers

Marloes Schoone

4th of August 2025

Thesis Committee:
Dr. Poulumi Dey (Supervisor)
Dr. Nabil Khossossi (Supervisor)
Dr. Kevin Rossi (External Committee Member)

TU Delft Delft University of Technology

Abstract

Sodium-ion batteries as an alternative to lithium-ion batteries are a promising candidate due to the cost-effectiveness, abundance and safety of sodium when compared to lithium. A major drawback is that sodium is not capable of intercalation in graphite. This study examines the viability of $NHCH_3$-Benzene, Aminobenzene and Phenol as spacers between graphene layers for use as a battery electrode. These spacers were chosen for their ability to create space between graphene layers for sodium, as well as activating the host structure for a stronger attraction to the sodium ions. Using Density Functional Theory (DFT), the structures were relaxed to their most stable configuration and loaded with sodium atoms to observe the effect of spacer material on atom behaviour. The aminobenzene spacer was identified to be the most attractive option from the tried materials in this study, both in formation energy and atom behaviour, as well as being an easily available material. Additionally, the effect of the starting positions of the inserted atoms before structure relaxation was tested. The starting position was found to directly influence the configuration of the sodium atoms in the host structure after relaxation, but the most stable positions close to the spacer were always filled, regardless of starting positions.

Contents

1 Introduction

Explosive electric vehicle market growth in the last 10 years[1] and growing grid instability due to fluctuating sustainable energy sources[2] have propelled the search for sustainable battery materials. With lithium-ion and lead-acid batteries dominating the market in the past, there has been a limited diversity in the available batteries and the focus of battery research. Concern for safety, scarcity and toxicity of lithium has opened the door to other battery materials. Recently, sodium-ion batteries have become more important and are already being used in Japan for electrical grid applications.[3] Layered oxides with sodium were previously one of the most studied positive electrode materials until the commercialisation of the lithium-ion battery. Sodium is one of Earth's most abundant materials, and has highly conductive ions at intermediate temperatures. Furthermore, lithium and sodium are both alkali ions, although sodium is bigger than lithium, which means that the research and materials originally used for lithium can now be evaluated for sodium.[4] For example, graphene is already one of the most used negative electrode materials in Li-ion batteries, which makes it an interesting starting point for sodium as well. However, due to the larger size of sodium, adaptations need to be made. Research into adding various structures, or spacers, to the graphene network to create space for the ions was performed, with promising results.[5–7] Such a spacer can have a dual function as it can physically create more space for sodium ions, or other larger alkali ions, while also chemically activating the host structure, causing stronger attraction to the alkali-ions. A stronger attraction between ions and electrode material can have a positive effect on the energy density and charging speed of a battery.[8] Learning more about the effect of activating spacer materials might facilitate the search for sustainable battery materials, especially when attempting to replace lithium with another, less electronegative alkali-ion. This study will focus on three of these possible spacer materials.

The main research objective of this study is to determine the viability of $NHCH_3$-Benzene, Aminobenzene and Phenol as spacers between graphene layers for use as a battery electrode. To achieve this, the following steps are taken:

- The material selection process is analysed.
- Adsorption and formation energies of the structure are calculated.
- Adsorption energies of sodium atoms loaded into the structure are determined.
- The effect of functional group orientation on a benzene ring is observed.

The secondary objective is to investigate the importance of the experimental setup of the DFT study on sodium atom behaviour and adsorption energies. This will be attempted by:

- Investigating several starting positions for the inserted atoms and considering the effect on the preferred position.
- Repeating part of the research done by Sun et al. on Janus-Graphite to compare data achieved in two different DFT studies.
- Evaluating the effect of using a 1 or 2-layer structure on sodium atom behaviour.

First, the theory behind alkali-ion batteries and the suitability of sodium as an alternative to lithium are discussed in Section 2.1, with a short introduction on rechargeable batteries and a discussion on ion storage mechanisms and electrode materials. Then, Section 2.2 considers Density Functional Theory (DFT), its theoretical background in quantum mechanics and its application in graphene functionalization for battery applications. Three case studies are considered (Section 2.3), Janus graphite created by Sun et al. (2021),[5] Antraquinone functionalized graphene created by Rasheev et al. (2020),[6] and pillared graphene created by Peymanirad et al. (2024).[7] The methods used in this study are elucidated in chapter 3. In Chapter 4, the results of the research objectives are presented and discussed. The conclusion and recommendations can be found in Section 5 and 6.

2 Theory

2.1 Sodium-ion as an Alternative to the Lithium-ion Battery

The increase in battery research due to electric vehicles and the worries about scarcity, toxicity and safety of lithium has led to extensive research into sodium-ion batteries.[4,8] To understand the materials suitable for use in these metal-ion batteries, one needs to understand how a rechargeable battery functions and how the chemical processes taking place during the transport of the ions work. The basic build-up of a rechargeable electrochemical cell is shown in Figure 1. The cell consists of two electrodes, an anode and a cathode, separated by an electrolyte, between which the chemical reactions take place. If necessary, a separator is added between the cathodes to avoid contact. Lastly, the electrodes are usually connected to a current collector, to allow for a connection to the power supply for charging. The ions interact with both electrodes as well as the electrolyte. Both of these materials have a great impact on the workings of the battery. Material requirements for the positive and negative electrode of the cell are very similar. They will need to be low in mass and/or volume depending on the application, they will need to be electrically conductive, and they need to withstand many battery loading and unloading cycles. However, the two electrodes need to have a difference in potential to encourage ion transport, with enough difference to avoid dendrite formation.[4] Thus, in a battery cell, two compatible electrodes need to be chosen. The electrolyte will not be further discussed as it lies outside the scope of this study. The following section will focus on ion storage mechanisms as they are very important for the effectiveness of a battery, and the material choice is of great effect.[9,10]

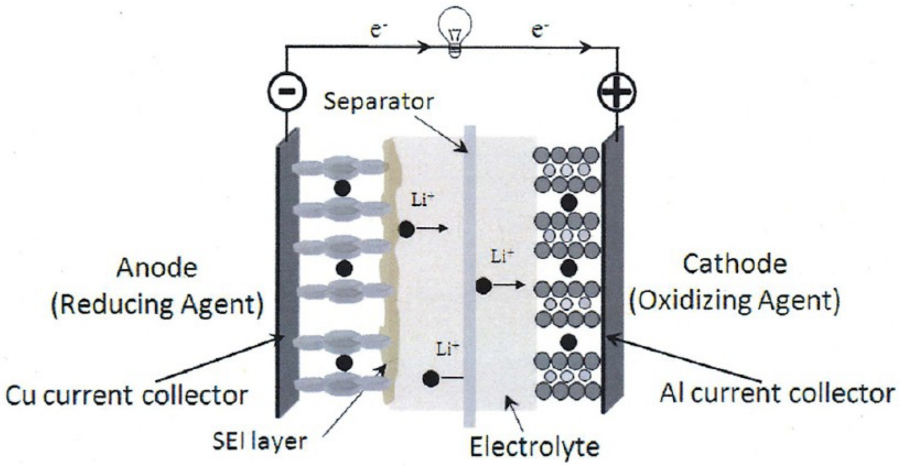

Fig. 1: Schematic representation of an electrochemical cell[10]

2.1.1 Ion Storage Mechanisms

The reaction mechanisms found in different electrodes are shown in Figure 2. Three mechanisms can be identified, namely insertion, alloying, and conversion. Insertion, more commonly known as intercalation, is the process where the ions move into free interstitial spaces in the host structure. Figure 2A shows this mechanism. The capacity is relatively low and depends on the host material and the ions. The intercalated structure can expand in volume. A lot of research has been done on this topic and it is currently the most used technique in metal-ion batteries.[8] As a second mechanism, ions can react with the host's structure by alloying (figure 2B). Here, the ion will form an alloy with a metallic or semi-metallic host material at room temperature. Compared to intercalation, this method has a very large capacity for ions, but volume change is still an unresolved issue, making it less ideal for use in batteries. The last mechanism is ion conversion, shown in Figure 2C, where the reaction of the ions with the host material will lead to nanoparticles embedded in a matrix. Similar to alloying, a large capacity is theoretically possible, but the technique is not yet used in commercial batteries. They are not yet very energy efficient, due to a large voltage hysteresis between charging and discharging.[4,8]

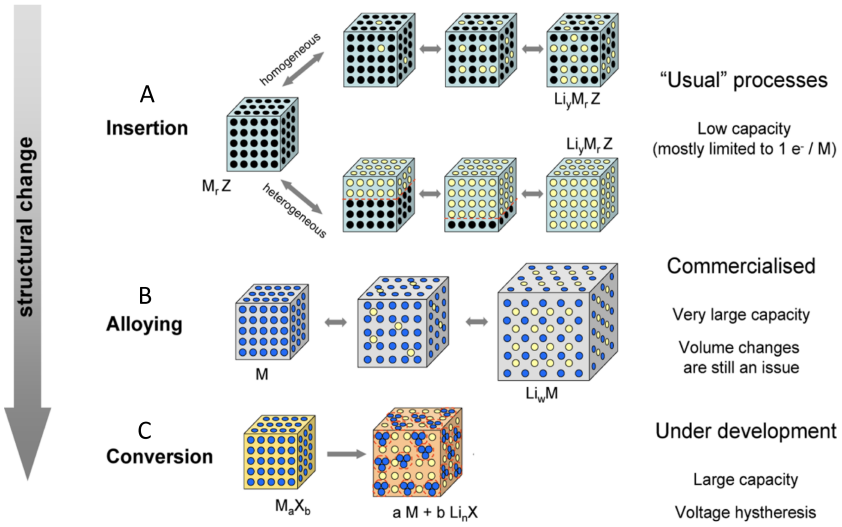

Fig. 2: Three reaction mechanisms in electrode materials. Black circles are voids in the crystal structure, blue circles are metal (M), and the yellow circles represent lithium. A) Insertion is the most common process, where the ion will occupy a free interstitial space. B) Alloying is when the host structure and the ion react to form an alloy. And C) Conversion is when the ions interact with the host material, leading to a matrix material with nanoparticles.[4]

Insertion Electrodes

Intercalation is an important part of the storage of ions. This chemical process is especially interesting as the intercalation of the ions in the host will have an effect on the properties of the host. Which properties are affected and to what degree depends on both the ions and the host material. The bonding between the ion and host material can also differ, depending on the materials, with Van der Waals, ionic or metallic bonds. Generally, the host lattice expands to accommodate the guest ions. As this process takes energy, 'staging' occurs as shown in Figure 3. Staging means that the intercalation process will occur in discrete steps. In this case, to move from one stage to the next, an entire row of ions exits and reintercalates as shown in Figure 3, where the 3rd stage has every 3rd layer filled with ions, the 2nd stage has every other layer fille,d and the 1st stage has every layer filled with ions. Although the structures during staging can be three-dimensionally ordered, generally the ordering is only in layers, as shown in the figure. With a lower intercalation energy, the energy necessary to insert or extract ions from the host material, only fully occupied layers are found, as the intercalation bonds will contribute to a large part of the intercalation energy. However, with a higher intercalation energy, partial occupancy of the occupied layer can be expected. The total free energies of the intercalation are relatively similar, but a higher free energy does lead to a higher theoretical energy density.[11,12]

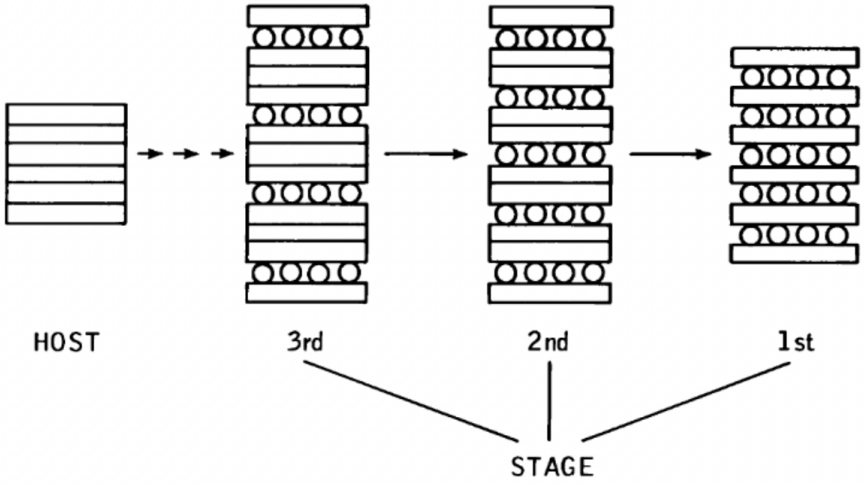

Fig. 3: Stages during intercalation. The host material has a layered structure, and during intercalation, the structure is filled with ions in the pattern described in the figure. First, the 3rd stage is filled, with every 3rd layer filled with ions, then the 2nd stage is filled, with ions on every other layer. Finally, in the first stage, the ions have filled every layer of the material.[12]

Alloying Electrodes

In the early 1970's it was discovered that alloying reactions at room temperature between lithium and metallic or semi-metallic bulk materials were possible.[13] In contrast to intercalation materials, the ion will alloy with the active electrode material, changing the structure from the host structure, a pure metal or alloy, to a host-ion alloy. This change in structure will lead to volume expansion upon loading and volume reduction at unloading. This can eventually lead to the pulverisation of the material. Volume expansion, however, is intrinsic to the alloying process, and the ensuing physical degradation is still the main issue in alloying electrodes and the focus of much research. Aside from the physical degradation of the electrode due to the expansion and contraction during loading and unloading, a further persisting problem is the loss of electrical contact during the loading process. This can either be caused by the volume expansion itself or the phase transitions in non-solid solution electrodes. To solve these issues, research focuses on alternatives to bulk materials that can minimise or accommodate volume changes while retaining their good capacity.[13–15]

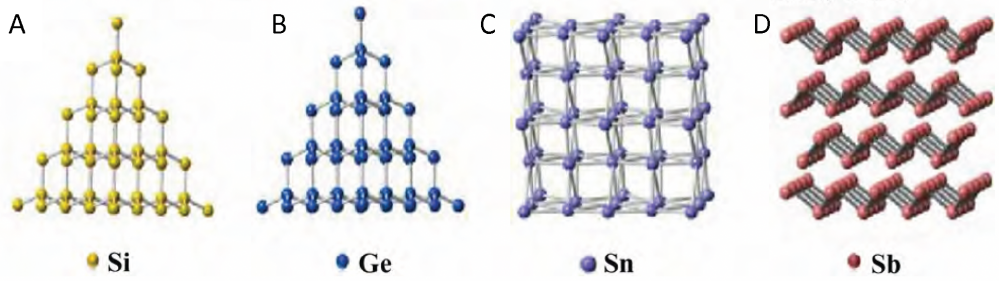

Fig. 4: Crystal structures of 4 materials currently used in alloying electrodes, namely A) silicon, and B) germanium, both with a diamond structure, C) tin with a cubic structure and D) antimony with a layered structure. All structures have space for ions to be inserted.[16]

The materials currently used as active materials in alloying electrodes for lithium and sodium are silicon, germanium, tin and antimony. Silicon is the most used material as it has the highest volumetric and gravimetric capacity.[17] Both silicon and germanium have diamond structures as shown in Figure 4A and B. Tin has a cubic structure, Figure 4C, and antimony has a layered structure as shown in 4D. All these crystal structures have space for ions to be inserted and alloyed. Silicon and tin are very abundant elements and are thus good choices in terms of availability. Especially antimony is used less as it is a much rarer element. Due to their electronegativity, all these 4 elements could be suitable as alternatives to a lithium ion battery if they offer suitable storage capacity.[8,18]

Conversion Electrodes

The first working conversion material was produced by Poizot et al. (2000),,[19] sparking much research on conversion compounds for battery applications. For the conversion electrode, usually a transition metal compound is used. Equation 1 shows the reaction that happens during conversion, with M the transition metal, X an anionic species and A the alkali ion. a, b, and c are the amount of atoms and e^- indicates the electron. Upon loading, the alkali ion will bind with the anionic species, and the transition metal is fully reduced to its metallic state.[20]

$$M_aX_b + bcA^+ + bce^- \rightleftarrows aM^0 + bA_cX \tag{1}$$

The transition metal is often iron, cobalt, nickel, copper or manganese, creating a transition metal compound together with anionic species such as oxides, sulphides, fluorides or nitrides. Conversion electrodes have theoretical capacities that are significantly higher than intercalation electrodes, and potential compounds that exist in natural forms, allowing for low production costs.[21] However, they have relatively low conductivity, high volume expansion and electrolyte decomposition. Similar to alloying electrodes, these disadvantages are extremely limiting for use as an electrode without modifications.[16]

2.1.2 Sodium Ion batteries

Positive Electrode

Already in 1981, Delmas demonstrated the reversibility of Na_xMnO_2 (NMO), indicating the layered oxide for possible use as an insertion electrode.[22] Figure 5 shows some of the layered oxide structures. Recently, the P2 structure for Na_xMnO_2 was found to have the largest energy density for a sodium ion battery.[8] Moreover, in the O3 structure, the ions need to move through the narrower tetrahedral centres, leading to a low diffusion rate. While in the P2 structure, the diffusion channel is larger, and a higher diffusion rate can be observed.[23] However, when layered oxide structures are used with larger alkali-ions than lithium, often the intercalation process can cause the transition metal layer to slip. For example, the O3, P3 and O1 structures in Figure 5 can easily transform into one another by the slabs gliding or slipping, and with larger ions the interactions between the oxide layers are decreased, thus leading to a less stable structure. Although technically fully reversible, it can cause volume changes, phase transition and possibly collapse of the structure. Additionally, the

high sensitivity to air and reactivity with moisture that layered oxides exhibit can lead to further instability.[24]

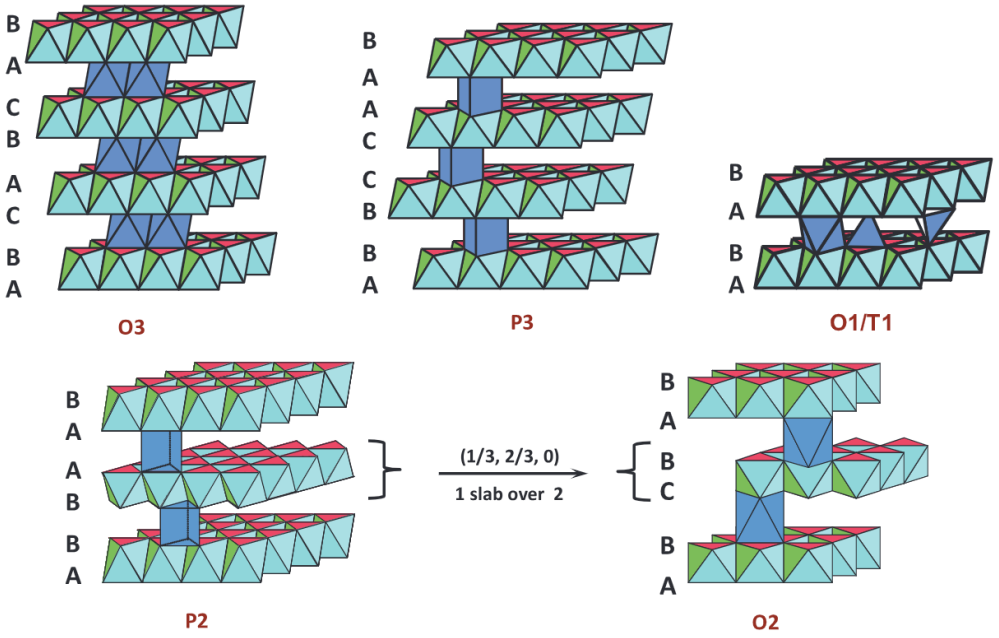

Fig. 5: Structures of layered oxides, with light blue the transition metal, and dark blue the alkali-ion. The O3, P3, and O1 structures can move from one to the other due to 'slipping' of the transition metal layer.[25]

Doping can be used to tune the properties of the electrode material and to improve mechanical stability and performance. The effects can vary greatly, depending on which sites are occupied by the dopant. Magnesium is an interesting option for doping, as it is non-toxic, lightweight and low-cost. In the case of magnesium, doping of the transition metal sites can lead to increased ion transport, while doping alkali-metal sites may increase stability. Different or multiple dopants will again lead to different effects on the properties, and could potentially lead to an incredibly tuned electrode material. However, the synthetic process of doping is a limiting element, as site-accurate and controllable doping is still hard to achieve.[26,27] Spinel oxides are a further valid option for use with sodium ions, as the Nasicon (Na super ionic conductor) type structure had already been discovered by Goodenough and Hong in 1976 and has been of renewed interest in the last few years in the search for alternatives for lithium batteries.[28,29] $NaFePO_4$ (NFP) is a spinel Nasicon structure and can be used as the positive electrode, having a good energy density to compete with lithium-ion batteries.[30]

Both sodium and potassium have successfully been used in alloying electrodes.[31] However, similar to the previously mentioned electrode, there are issues with volume expansions as well as with reversibility due to voltage hysteresis. The theoretical capacity is high but has not yet been reached by a researched material. Much is still unclear about the electrochemical behaviour of the produced materials and cell design, electrolytes, and binders must be further researched.[32,33]

Iron oxide materials are popular for use in conversion electrodes due to their good specific capacity, low cost, abundance and non-toxicity.[34] An especially interesting one is Fe_3O_4, as it can be found in nature. However, there are still problems with stability and capacity decrease over time.[34] Mixed transition metal compounds could overcome some of the problems mentioned before, increasing the stability of the electrode material. An interesting example for the positive electrode is NMC, which has a combination of nickel, manganese and cobalt in an $\alpha - NaFeO_2$ layered structure. With its high charge capacity and rate capability as well as structural stability, NMC makes for a cheaper alternative to the standard insertion electrodes. However, it can undergo mechanical instability at the surface of the electrode.[35,36] Instead of tuning the properties of the conversion compound by choosing multiple transition metals, multiple anionic species can be used instead. For example, the positive electrode material $FeOF$ uses the high energy density caused by adding fluorine, and adds oxygen to decrease hysteresis and improve the kinetics of the compound. To improve rate capability, or how well a battery can deliver power, the material is formed of nanorods. To prevent side reactions with the electrolyte, the nanorods are coated in a nanolayer of a conducting polymer, PEDOT.[37]

Negative Electrode

There is already abundant promising research for positive electrode materials for use with sodium, although there are still various obstacles regarding stability and reversibility. However, the true restricting factor is the negative electrode.[8] Most of the lithium-ion batteries on the market use graphite as the negative electrode, due to its relatively low cost, high energy and power density and long cycle life. Graphite is also being researched extensively for use as a negative electrode for batteries with alternative alkali-metal ions. Similar to the materials mentioned above, the lithium ions intercalate into the graphite electrode, creating a Graphite Intercalation Compound or GIC. The graphene layers are connected with Van der Waals bonds, whose weak interaction allows for the intercalation of ions. The bonds between the carbon atoms in the layer are strong, thus, the graphite lattice will be retained. However,

when larger alkali-ions are inserted, the intercalation process moves more slowly, and fewer ions can be inserted.[12,38] There is not yet one theory that can explain the differences in staging (figure 3) between the different alkali-ions. The effect of the size of the ion is often used to explain why lithium intercalates so well. The smaller lithium would allow lithium-graphite materials to generally form as LiC_6, LiC_{12} or LiC_{18} which are respectively intercalation stages 1, 2 and 3.[39] Larger ions such as potassium, rubidium and caesium intercalate to stages 1, 2, 3, 4 or 5, with for example, potassium, respectively in compositions KC_8, KC_{24}, KC_{36}, KC_{48}, KC_{60}.[40] The exception here is sodium, as while it is smaller than potassium, it intercalates into graphite less easily with a most intercalated composition of NaC_{64}.[41] Although recently there has been a lot of research done into the mechanics behind graphite intercalation, the thermodynamics and kinetics are not entirely clear yet and require further study.[38] It is likely that the behaviour of the sodium ions is caused by a relatively large ionic radius combined with an ionisation potential that is relatively low.[5] However, sodium is an interesting material due to its good availability, resulting in a search for solutions to its less optimal intercalation. Two methods stand out, namely co-intercalation and artificially increasing the graphene layer distance. Firstly, co-intercalation uses solvated ions. By solvating the ions the intercalation efficiency is improved. Secondly, functionalizing the graphene surface with atoms or molecules allows for tuning of the necessary intercalation properties. The next section will discuss functionalized graphene further.

2.1.3 Functionalized Graphene

Functionalising the graphene surface can be done using atoms or molecules, or a combination of both. In 2004, Noselov et al.[42] managed to create monocrystalline graphitic films for transistor applications. Their discovery allowed for exploration into the optimisation of mono or few-layer graphite for electrode properties as well. A prevalent example of functionalised graphene in electrode materials is Graphene Oxide (GO), as shown in Figure 6. GO is simply an oxygenated layer of graphene, and was historically a step in the synthesis of graphene, rather than an interesting material in itself. However, recent research shows that negatively charged 'OH' and 'O' groups on the GO surface attract the metal cations, accelerating ion transport. Additionally, the functional groups can repel a same-charge electrolyte to prevent corrosion.[43,44]

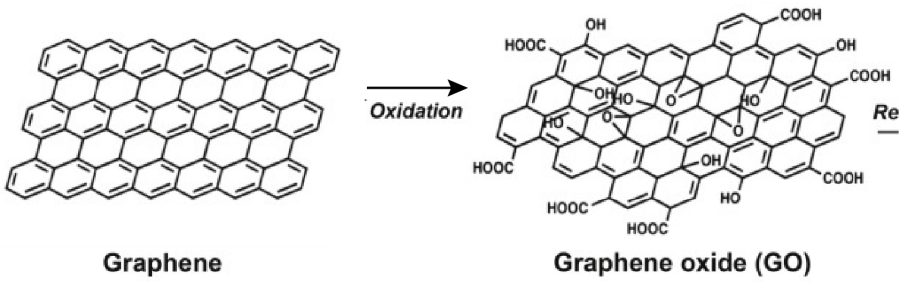

Fig. 6: Schematic view of graphene and graphene oxide, adapted from McCoy et al. (2019).[45]

Functionalizing the surface of graphene with atoms can be achieved by two methods. The first is heteroatom doping or co-doping, where some of the C atoms are replaced by respectively one or more types of atoms. The second way is to attach dopants onto the surface, similar to GO. The choice of which atom or atoms are used to dope the surface can greatly affect the properties of the material, both positively and negatively. Thus, it is important to choose atoms that will only disrupt the graphene structure enough to cause the effects needed, but not so much that the structure becomes unstable. Accordingly, atoms with similarities to carbon, such as nitrogen, boron, phosphor and sulphur are seen as most suitable for stable doping of the graphene surface.[46,47] Nitrogen-doping of graphene is especially interesting as it can lead to three distinct structures with the nitrogen atom bonding differently to the graphene surface. Each structure behaves differently due to the effect of the nitrogen atoms on the neighbouring carbon atoms. Capacitance, conductivity as well as electrochemical performance can be improved, and the band gap can be tuned.[48–50]

Attaching larger molecules to the graphene or doped graphene surface gives further interesting options, as aside from changing the electronegativity of the surface, similar to functionalizing with atoms and small molecules, larger molecules can also serve a structural purpose. Re-stacking of the graphene layers is generally attributed as the cause of the lower practical than theoretical capacitance, and molecular pillars can be used to control this, as well as the porosity of the material. Many different materials can be used, such as conducting polymers and redox-active molecules.[51–54] For example, by artificially increasing the graphene interlayer distance using molecular spacers, enough distance is created for larger alkali ions to intercalate. Sun et al. (2021)[5] created 'Janus-graphite' where an aminobenzene spacer is placed on top of the graphene sheet, minimising the Van der Waals interaction between the sheets and allowing for reversible sodium intercalation without staging, with a sodium-carbon ratio of $NaC_{6.9}$. The created structure is shown in Figure 7. A further review of

Janus-graphite can be found in Section 2.3.1.

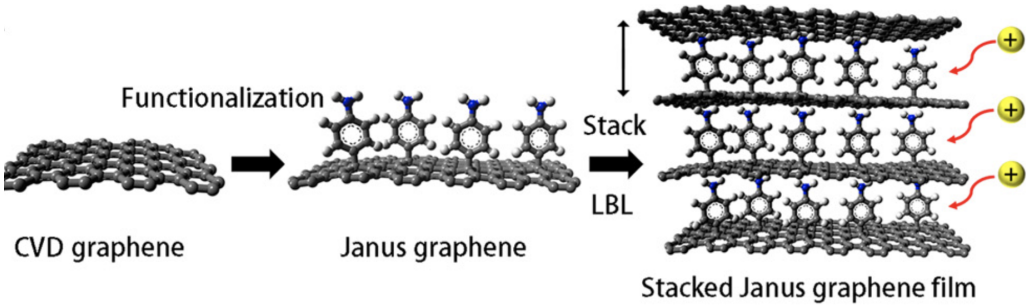

Fig. 7: Production and stacking of Janus-graphite. From left to right, the graphene layer is produced using Chemical Vapour Deposition (CVD), the Janus-graphene is formed by functionalizing the surface with aminobenzene spacers, and finally, the Janus-graphene is stacked Layer-by-Layer (LBL) to create Janus-graphite.[5]

2.2 Density Functional Theory

Density Functional Theory (DFT) is a computational method widely used to model the electronic structure of atoms, molecules and condensed matter systems. DFT calculations provide a good compromise between computational cost and accuracy, making it a standard tool in materials science, chemistry, and solid-state physics.[55] DFT is based on quantum mechanics, and the underlying theory will be introduced in Section 2.2.1. The different functionals used in DFT, such as the Local Density Approximation (LDA) and Generalized Gradient Approximtion (GGA), will be discussed in section 2.2.2.

2.2.1 Quantum Mechanics

Many-Body Problem

Particles on the quantum level were found to behave differently than classical physics described. Quantum Mechanics was necessary to describe the behaviour. The many particles that interact in a structure on a quantum level significantly complicate calculations, as any particle has interactions with any other particle nearby. Such a many-body problem can be described by the Schrödinger equation, shown in Equation 2). With $\hat{H}$ the Hamiltonian, further expressed in Equation 3, E the energy of the system and Ψ the wavefunction of the considered system. $\mathbf{r}$ and $\mathbf{R}$ describe the electron and nucleus coordinates respectively.

$$\hat{H}\Psi(\{\mathbf{r}_I\},\{\mathbf{R}_i\}) = E\Psi(\{\mathbf{r}_I\},\{\mathbf{R}_i\}) \tag{2}$$

$$\hat{H} = \underbrace{-\frac{\hbar^2}{2m_e}\sum_i \nabla_i^2}_{\hat{T}_e\{r\}} \underbrace{-\frac{\hbar^2}{2}\sum_I \frac{\nabla_I^2}{M_I}}_{\hat{T}_n\{R\}} + \underbrace{\underbrace{\frac{1}{2}\sum_{i\neq j}\frac{e^2}{4\pi\epsilon_0\mathbf{r}_{ij}}}_{\hat{V}_{ee}\{r\}} \underbrace{-\sum_{i,I}\frac{e^2 Z_I}{4\pi\epsilon_0\mathbf{R}_{iI}}}_{\hat{V}_{en}\{r\},\{R\}} + \underbrace{\frac{1}{2}\sum_{I\neq J}\frac{e^2 Z_I Z_J}{4\pi\epsilon_0\mathbf{R}_{IJ}}}_{\hat{V}_{nn}\{R\}}}_{\hat{V}} \tag{3}$$

The Hamiltonian can be divided into 5 terms, denoted below the terms in Equation 3. $\hat{T}_e\{r\}$ describes the kinetic energy of the electrons, $\hat{T}_n\{R\}$ describes the kinetic energy of the nuclei. $\hat{V}_{ee}\{r\}$ represents the repulsion of electrons, $\hat{V}_{en}\{r\},\{R\}$ the attraction between electrons and nuclei, and $\hat{V}_{nn}\{R\}$ the repulsion of nuclei. Most molecules and systems simply contain so many particles that solving these equations numerically is extremely complicated, and approximate equations have to be used.[56]

Born-Oppenheimer Approximation

The first level of approximation is the Born-Oppenheimer approximation. Since a nucleus is many times larger in mass than an electron, a nucleus would move much more slowly than an electron. This is exacerbated by the attractive force caused by the opposite charges of nuclei and electrons. This attractive force accelerates the particles, with the magnitude of the acceleration inversely proportional to the mass. Thus, the acceleration of the nuclei is small, while the acceleration of the electrons is large. The Born-Oppenheimer approximation, therefore, neglects the motion of the atomic nuclei, leading to the revised Hamiltonian in Equation 4.[57] Compared to the original Hamiltonian equation in Equation 3, only $\hat{T}_e\{r\}$, describing the kinetic energy of the electrons, $\hat{V}_{ee}\{r\}$ representing the repulsion of electrons, and $\hat{V}_{en}\{r\},\{R\}$ expressing the attraction between electrons and nuclei, are considered.

$$\hat{H}_e = \underbrace{-\frac{\hbar^2}{2m_e}\sum_i \nabla_i^2}_{\hat{T}_e\{r\}} + \underbrace{\underbrace{\frac{1}{2}\sum_{i\neq j}\frac{e^2}{4\pi\epsilon_0 r_{ij}}}_{\hat{V}_{ee}\{r\}} \underbrace{-\sum_{i,I}\frac{e^2 Z_I}{4\pi\epsilon_0 R_{iI}}}_{\hat{V}_{en}\{r\}\{R\}}}_{\hat{V}} . \tag{4}$$

Although the Born-Oppenheimer approximation is already a simplified situation, for many electrons, there are still numerous interactions. Therefore, another level of simplification is necessary, constraining the degrees of freedom in the observed system. The Hartree-Fock or Self-Consistent Field (SCF) approximation further breaks down the wave function of all electrons into single-electron wave functions. The repulsion between electrons is calculated by comparing each electron with an average field of all other electrons.[58]

2.2.2 DFT-functionals

Kohn-Sham

For Density Functional Theory (DFT), the Schrödinger equation was reformulated into Kohn-Sham equations.[59] Instead of each electron interacting with every other electron, the non-interacting Kohn-Sham particles generally allow for faster problem solving. The set of Kohn-Sham equations confines the unknown quantities into one function, the exchange correlation density functional, shown in Equation 5. E_{xc} represents the energy per electron, with $n(\mathbf{r})$ the electron density.

$$E_{xc}[n(\mathbf{r})] \tag{5}$$

However, the exact functional is unknown and has to be approximated. Many methods have been developed and depend on the system that is being considered. Thus, it is important to select the functional carefully as different cases require different approximations. Table 1 shows some of these different methods. Local Density Approximation (LDA) and Generalised Gradient Approximation (GGA) are most prevalent in materials research, combining good accuracy with high performance.[55] Furthermore, when using a structure such as a graphene network, it is essential to take the van der Waals interactions into account as well.

Name	*Parameters*
Local Density Approximation (LDA)	Electron density
Generalized Gradient Approximation (GGA)	Electron density and its gradient
Meta-GGA	The Laplacians of the density and/or kinetic energy densities are added
Hyper-GGA	The exact exchange is added
Generalized random phase approximation	The exact exchange and exact partial correlation are added
Subsystem functionals	Tailored functionals are used for different parts of the system
van der Waals interaction	The van der Waals interactions are added
Surface correction procedure	Exact surface energies are used

Table 1: DFT functionals and their considered parameters[60]

2.3 Case Studies

2.3.1 Janus Graphene

In search of a suitable negative electrode material for use with alkali ions larger than lithium, Sun et al. (2021)[5] designed and produced 'Janus-graphite', named for its asymmetric functionalization. The intercalation process (Figure 8A) was studied using operando Raman spectroelectrochemistry and DFT calculations. The graphene layers were synthesised using chemical vapour deposition, and functionalized using diazonium chemistry. 4-nitrobenzene diazonium tetrafluoroborate (4-NBD) was used as the first step to create the spacer. 4-NBD consists of a benzene derivative, with $-NO_2$ and $-N_2^+$ attached on opposite sides of the benzene ring. The benzene derivative is surrounded by BF_4^-. When the 4-NBD is grafted onto the graphene, the N_2 is detached from the benzene derivative and the gas is released. Using electro-

chemical reduction, the $-NO_2$ group is converted to $-NH_2$, to form nitrobenzene-functionalized graphene.

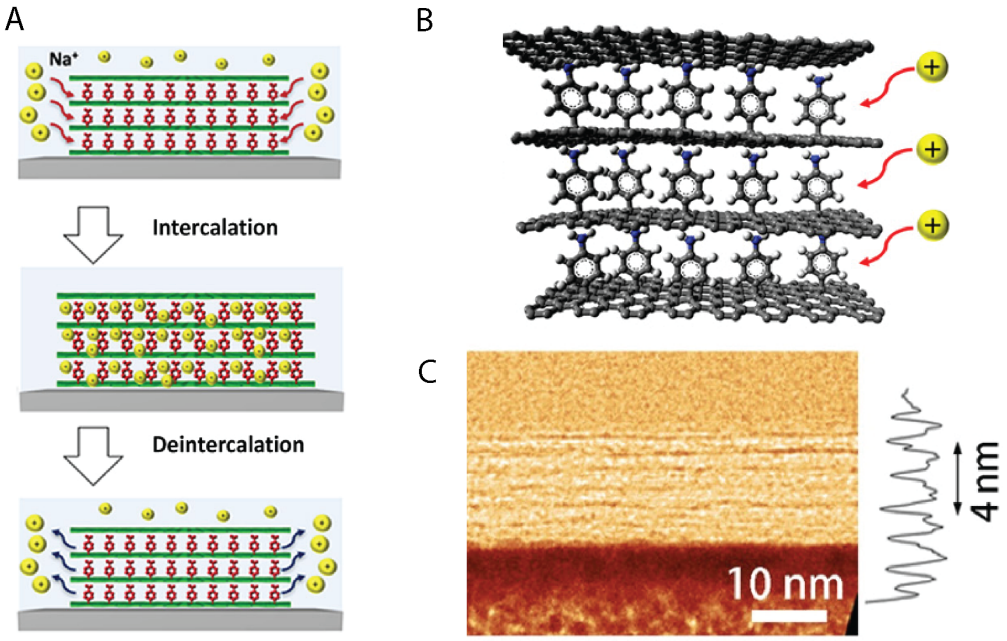

Fig. 8: Janus Graphene with A) the intercalation process, B) Schematic model and C) Cross-sectional high-resolution TEM image of stacked AB graphene thin film.[5]

After the creation of the functionalized graphene, it was stacked into a multilayer structure (Figure 8B). Figure 8C shows a Transmission Electron Microscopy (TEM) image of the layered structure. Due to the functionalization of the graphene, there was less interaction between the graphene sheets, allowing for better alignment than in pristine graphite. No cracks or wrinkles were visible. The created structure was also observed using DFT to gain further insight into the preferred configurations of the molecules. A 3D model of the nitrobenzene functionalized graphene was made and relaxed using DFT-D3. On top of the relaxed one-layer structure, a graphene-layer was stacked at multiple distances. An energy calculation was performed for each distance. Both the synthesised graphene sheets and the DFT calculations agreed on a preferred interlayer distance of around 1 nm. Further DFT calculations were performed for the insertion of sodium atoms, and Sun et al. found that the most favourable position for sodium was coordinated to the $-NH_2$ group of the spacer molecule.

2.3.2 Anthraquinone-Functionalized Graphene

Rasheev et al. (2020)[6] show the promise of anthraquinone (AQ)-functionalized graphene as a battery electrode material. Using DFT, they studied the electrochemical behaviour of their modelled material. To gain insight into the dynamics of ion insertion, Ab-Initio Molecular Dynamics (AIMD) was used to establish the most likely migration paths through the electrode material for Li^+. Firstly, the anthraquinone graphene structure had to be designed. Figure 9 shows this process. The attachment points (figure 9A) and orientation of the AQ attachment to the graphene surface (figure 9C) were tested and the most electronically stable configuration was chosen. Furthermore, the optimal loading of the graphene surface with the AQ molecule was calculated using the relative free energy of formation (Equation 6). The graphene layer loaded with the optimal amount of AQ spacers is shown in Figure 9B.

$$\Delta G_n = G(AQ_nC_{72}) - \frac{[nG(AQ_7C_{72}) + (7-n)G(C_{72})]}{7} \tag{6}$$

With G the total free energy and $n = 0 - 7$. It was calculated that no more than 7 AQ spacers could be added.

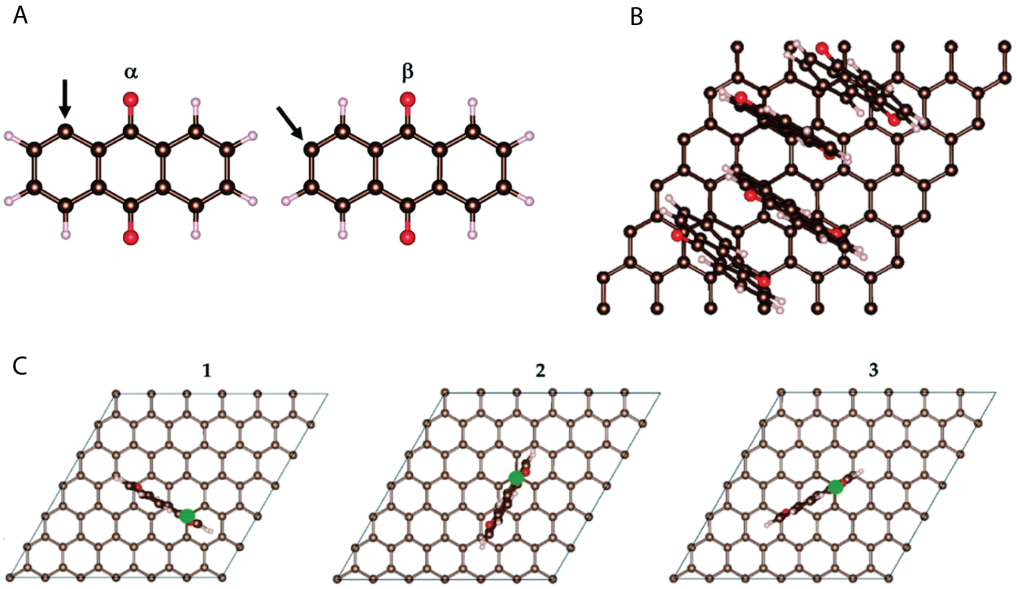

Fig. 9: Anthraquinone functionalized graphene with A) possible attachment points of the radicals, B) orientations of the radicals on the graphene surface and C) The final anthraquinone structure with optimal loading.[6]

After the structure was created, the atoms were inserted. Rasheev et al. considered Li, Ca and Al. The atoms were inserted one or two at a time to find the energetically most favourable configuration of atoms for each step. The atom loading was continued until the intercalation became unfavourable energetically. The behaviour of the loaded structures was analysed, and for Li, no expansion of the electrode material was observed upon loading. Moreover, no structural effects were detected due to lithium absorption at the surface. The loading became unfavourable at 16 atoms. The preferred positions for calcium were found to be similar to those for lithium, with a maximum of 8 calcium atoms. However, the distribution of the calcium atoms was less uniform, and the alignment of the AQ molecules was reduced. For the final element, aluminium, the structure could be loaded with up to 4 atoms, but the 3rd and 4th atoms provoked significant deformation of the structure. The charge transfer from lithium and aluminium to the AQ-graphene structure was 87-89%, while the charge transfer from calcium was around 75%. The calculated capacity and energy density for each material are shown in Table 2.

Metal	Capacity (AQ_4C_{72}), mAh/g	Capacity (AQ_4-only), mAh/g
Li	222	453
Ca	253	517
Al	95	194

Metal	Energy density (AQ_4C_{72}), Wh/kg	Energy density (AQ_4-only), Wh/kg
Li	279	570
Ca	251	512
Al	65	133

Table 2: Calculated theoretical specific capacity and gravimetric energy density of the electrode for Li^+, Ca^{2+} and Al^{3+}.[6]

Finally, to form a picture of the dynamics of the ions in the structure, AIMD simulations were performed. Diffusion paths were established and the corresponding activation barriers for ionic diffusion were evaluated. The diffusion coefficients and activation barriers for the diffusion paths are given in Table 3. The diffusion coeffi-

cient for lithium in the AQ structure is significantly lower than in a standard LIB, and the coefficients for Al^{3+} and Ca^{2+} are even lower. Rasheev et al. (2019) expect the kinetics to be the greatest obstacle for this electrode material, and they suggest that the final design of a successful organic-graphene electrode will most likely be very different from one made of traditional intercalation compounds as used here.[6]

	Li^+		Ca^{2+}		Al^{3+}	
Path#	E_a [kJ mol^{-1}]	D [m^2 s^{-1}]	E_a [kJ mol^{-1}]	D [m^2 s^{-1}]	E_a [kJ mol^{-1}]	D [m^2 s^{-1}]
1	84	$\approx 10^{-21}$	144	$\approx 10^{-32}$	202	$\approx 10^{-42}$
2	132	$\approx 10^{-31}$	142	$\approx 10^{-31}$	226	$\approx 10^{-46}$
3	79	$\approx 10^{-20}$	167	$\approx 10^{-36}$	166	$\approx 10^{-36}$

Table 3: Diffusion coefficients (D) and Activation barriers (Ea) for the diffusion paths of LI^+, Ca^{2+} and Al^{3+}.[6]

2.3.3 Pillared Graphene

Peymanirad et al. (2024),[7] have created a graphite structure where the graphene layers are connected by pillars. The structures were relaxed using DFT-D3, and the adsorption energies of sodium at several locations were calculated. Ab initio molecular dynamics (AIMD) simulations were used to validate the chemical stability. Two structures were created and optimised, shown in Figure 10. MPG-I consists of a graphene and naphtalene pillar between two AA stacked graphene sheets (figure 10b), with an interlayer distance of 14.4 Å. MPG-II is made from pyrene sandwiched between AB stacked graphene layers (figure 10c), with an interlayer distance of 12.2 Å. Peymanirad et al. identified several unique adsorption locations for the sodium ions, shown by * in Figure 10. H1, H2 and H3 all represent hollow sites at the centre of graphene rings, B1 describes a site above the bond between two carbon atoms, and T1 and T2 are coordinated directly above carbon atoms. All of these sites are located along the pillar. Furthermore, on the graphene layer, a site in the middle of the carbon ring, O, and a site on top of the bond between two atoms, O' can also be identified. For the MPG-I and MPG-II structures, all the adsorption sites are shown in Table 4, with the distances to the closest carbon atom, distance to the graphene layer and adsorption energy specified. The T1 site has the lowest adsorption energy for both structures, indicating that this is the preferred position for sodium adsorption.

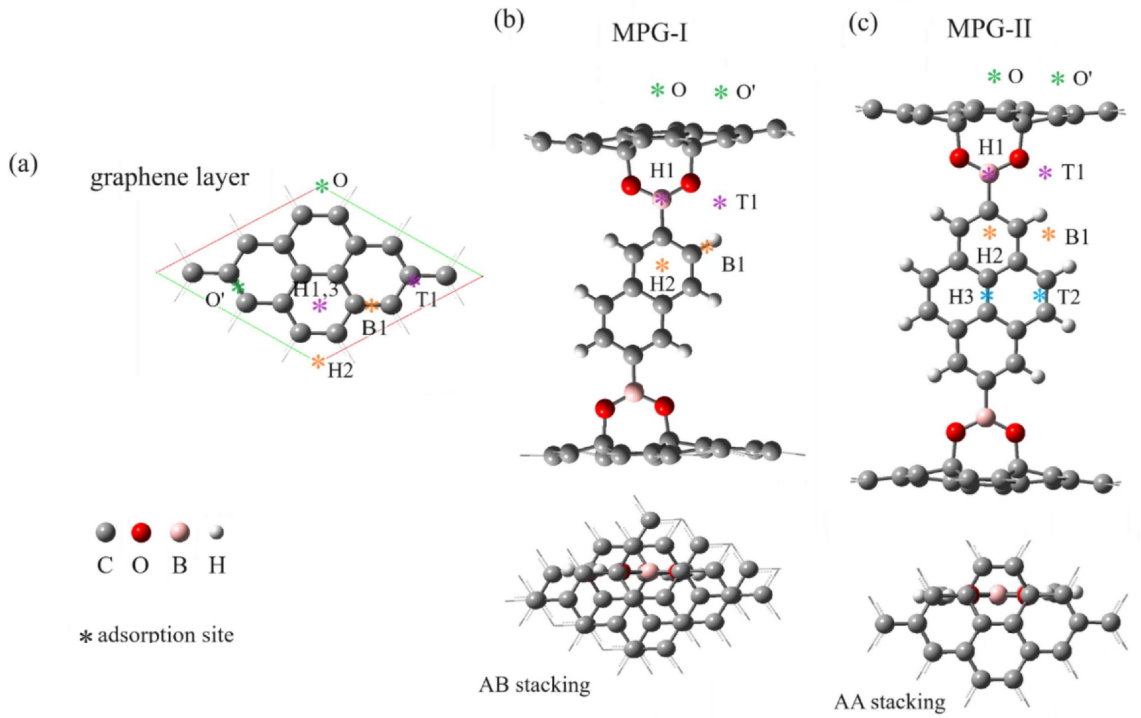

Fig. 10: 3D model of (a) the graphene layer, (b) MPG-I and (c) MPG-II. The sodium adsorption sites are shown by *.[7]

When loading the structures with more sodium atoms, it was found that the MPG-I can hold 12 atoms before the sodium starts to cluster, with a further 8 atoms adsorbing on the O and O' sites on the graphene layers, leading to a total of 20 adsorbed sodium atoms. MPG-II can hold 15 atoms, with another 8 atoms on the graphene layers, giving in total 23 adsorbed sodium atoms. Diffusion pathways between the adsorption sites were tested using AIMD. The pathway between the two most stable adsorption positions, T1 and H1, was found to have the lowest diffusion barrier, at 0.6 eV. To learn about the thermal stability of the structures, AMD simulations were conducted at ambient temperature. The total energy exhibited minimal fluctuations and the structures were maintained. Lastly, the open circuit voltage (OCV) was calculated, using Equation 7.

$$OCV = \frac{E_{MPG} + n_{Na}E_{Na} - E_{MPG+Na}}{n_{Na}e} \tag{7}$$

with E the energy, n_{Na} the number of adsorbed sodium atoms and e the Adatom charge (1 for Na^+). Average OCV values below 1.5 V were observed, which is within

the optimal voltage range for anode materials for sodium ion batteries. Peymanirad et al. indicate that the favourable properties found for the MPG materials as pillars between graphene layers suggest that these structures might have the necessary characteristics for use in high-performance batteries.[7]

structure	**MPG-I**			**MPG-II**		
Adsorption site	$d_{\text{Na-C}}$ **(Å)**	$d_{\text{Na-graphene}}$ **(Å)**	E_{ads} **(eV)**	$d_{\text{Na-C}}$ **(Å)**	$d_{\text{Na-graphene}}$ **(Å)**	E_{ads} **(eV)**
T1	2.6	2.6	−2.15	2.5	2.5	−1.67
H1	2.8	2.4	−1.56	2.7	2.4	−1.20
B1	2.4	4.9	−1.02	2.4	4.7	−0.58
H2	2.6	5.2	−0.98	2.5	4.8	−0.50
T2	–	–	–	2.7	7.5	−0.21
H3	–	–	–	2.5	7.5	−0.34
O	3.3	2.8	−0.15	3.4	2.8	−0.38
O'	2.9	2.8	−0.28	2.8	2.7	−0.50

Table 4: The distance of Na^+ to the nearest C, the distance of Na^+ to the graphene sheet, and the adsorption energy for Na^+ at various adsorption sites on MPG structures. The adsorption sites correspond to those shown in 10.[7]

3 Methods

The tools and methods used in this study are discussed in this chapter. The software used for the creation of 3D models is discussed in Section 3.1. The visualisations for this thesis were mainly created using VESTA, which can be found in Section 3.2. The software and inputs for Density Functional Theory calculations are discussed in Section 3.3. The various analysis methods used during this study can be found in Section 3.4.

3.1 Atomic Simulation Environment

For the construction of the 3D models, the Python library 'Atomic Simulation Environment' (ASE) was used.[61] ASE is a tool for creating, visualising and analysing 3D models. Although it can also run simulations, this function was not used.

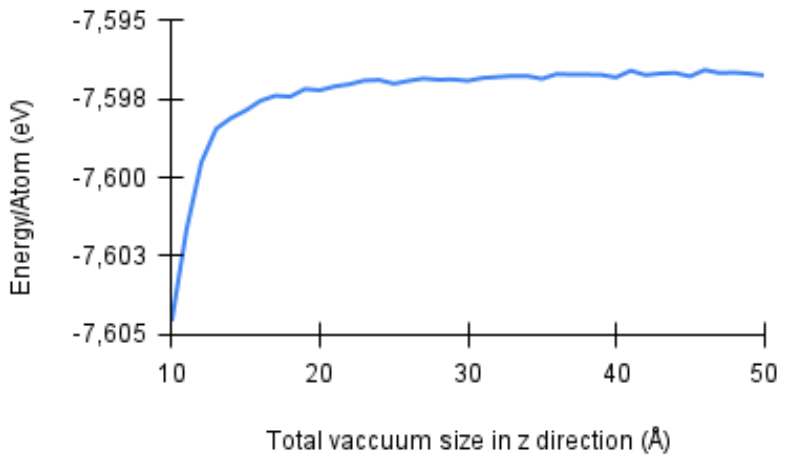

Fig. 11: Convergence test for vacuum height on a 3x3 graphene layer with a $NHCH_3$-benzene spacer, dataset can be found in Table 15 in Appendix A.

The structures were built by creating a graphene layer and attaching a pre-made molecule in the cases of the aminobenzene[62] and phenol[63] structures. The pre-made structures were downloaded from the NIH 3D database. The $-NHCH_3$ structure was created using ASE. The created structure was placed in a vacuum box in the z direction with a total height of 30 Å, which leaves around 20 Å of unfilled vacuum space to isolate the structure from its periodic images. The vacuum size was established using a convergence test from a total vacuum height between 10 and 50 Å, shown in figure 11.

3.2 Visualization for Electronic and Structural Analysis

Visualisation for Electronic and Structural Analysis, better known as VESTA, is 3D visualisation software for structural models.[64] VESTA was used to create images of the 3D models and to calculate and visualise the differential charge density, which is further discussed in Section 3.4.1. All of the 3D models in this thesis were made using VESTA, unless otherwise specified. When sodium is shown in a figure, an ionic radius of 1.02 nm was used.[65]

3.3 Vienna Ab initio Simulation Package

Vienna Ab initio Simulation Package (VASP)[66] was the software used to perform the Density Functional Theory (DFT) calculations. The input files and values are discussed in the following sections.

3.3.1 INCAR

The INCAR file defines the parameters of the DFT calculation. Although many of the values have default settings when left unspecified, the tags discussed here were specified at throughout this research to ensure consistency. The next section discusses all tags shown in the example INCAR file in Figure 12.

```
ENCUT = 550          # Plane-wave cutoff (eV)
PREC = Accurate      # High precision
EDIFF = 1E-6         # Electronic convergence
ALGO = Normal        # Standard SCF

# Ionic relaxation
ISIF = 2             # Relax ions
IBRION = 2           # Conjugate gradient
NSW = 200            # Max ionic steps
EDIFFG = -0.02       # Force convergence (eV/A)

# Exchange-correlation
GGA = PE             # PBE functional
IVDW = 12            # DFT-D3 for MOF dispersion

# Smearing
ISMEAR = 0           # Gaussian smearing
SIGMA = 0.05         # Small smearing

NCORE = 32
KPAR = 2

# Output
LCHARG = .FALSE.     # No CHGCAR
LWAVE = .FALSE.      # No WAVECAR
```

Fig. 12: Example of an INCAR file used for structure relaxation.

ENCUT

The ENCUT tag specifies the energy, E_cut, where the plane wave basis set is cut off as defined by Equation 8.[67] **G** denotes the reciprocal lattice vector, and **k** the wave vector.

$$|\mathbf{G} + \mathbf{k}| = G_{cut} \text{ with } E_{cut} = \frac{\hbar_2}{2m} G_{cut}^2 \tag{8}$$

The optimal value for use in this study was chosen by running a convergence test on a 3x3 graphene surface with a $NHCH_3$-benzene spacer attached. The total free energy was calculated for every 25 eV between 200 eV and 1000 eV, the corresponding graph is shown in Figure 13. An ENCUT value of 550 eV was chosen.

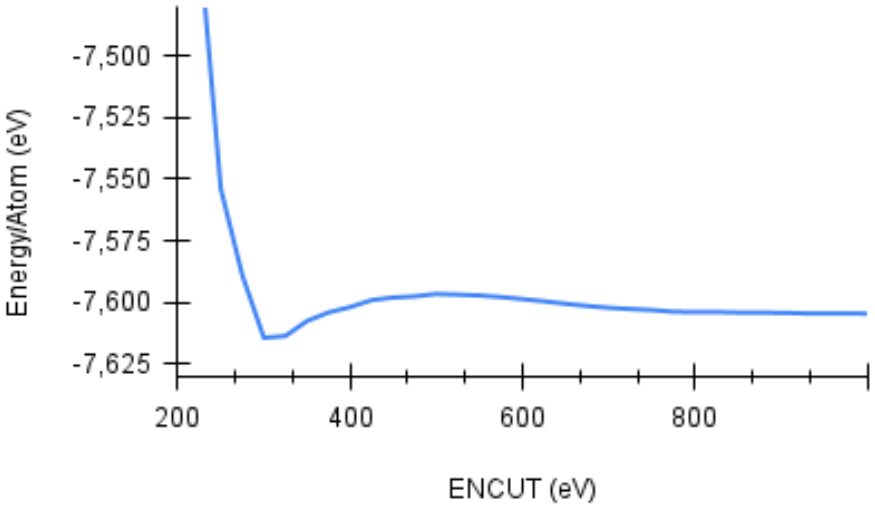

Fig. 13: Convergence test for ENCUT on a 3x3 graphene layer with a $NHCH_3$-benzene spacer, dataset can be found in Table 11 in Appendix A.

PREC

The PREC tag specifies the precision used in the calculation by setting default values for the cut-off energy, augmentation fine grid (NGXF,NGYF,NGZF) and the pseudo-orbitals grid (NGX,NGY,NGZ). Since the cut-off energy is specified in this study, it will not be affected by this tag. The 'Accurate' input used here sets the augmentation fine grid to be twice as large as the pseudo-orbitals grid.[68]

EDIFF

EDIFF defines the value at which the electronic self-consistent (SC) loop breaks. The change in total free energy and band structure energy between two steps in the SC-loop must be smaller than EDIFF. For a well-converged calculation, the EDIFF value must be low enough to ensure accurate results.[69] Figure 14 shows the convergence test run for EDIFF for the 3x3 graphene layer with $NHCH_3$-benzene spacer also used for the ENCUT convergence test. The convergence of the system was tested for EDIFF values between 1 and 10^{-10}.

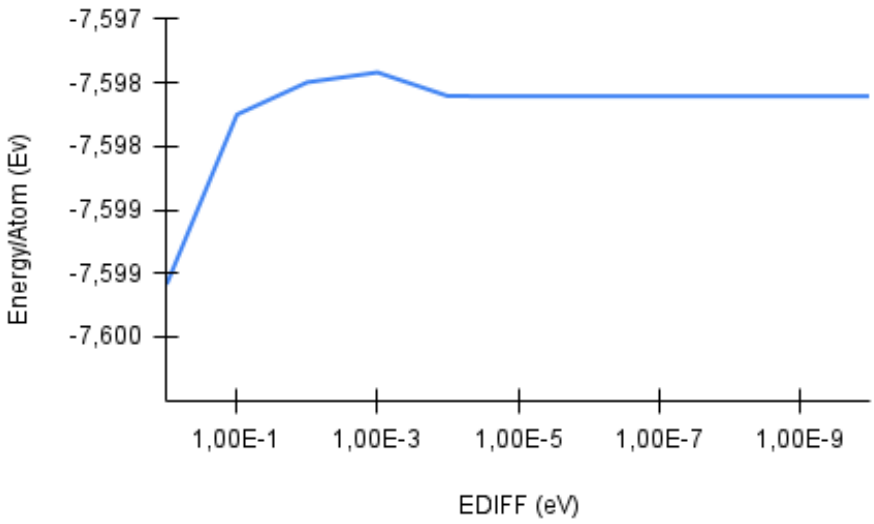

Fig. 14: Convergence test for EDIFF on a 3x3 graphene layer with a $NHCH_3$-benzene spacer, dataset can be found in Table 12 in Appendix A.

ALGO

The ALGO tag is used to select the electronic minimisation algorithm and the type of GW calculation. Setting ALGO to 'Normal' is used for a standard Self-Consistent Field (SCF) calculation. It makes use of the blocked-Davidson iteration scheme.[70]

ISIF

ISIF specifies the degrees of freedom of the structure during relaxation and determines whether the stress tensor is calculated. Table 5 shows which ISIF values control the stress tensor calculation and if the atom position, cell shape and cell volume are allowed to change. For this study, an ISIF value of 2 was chosen, allowing the atoms

to move while preventing the cell from changing shape or volume. ISIF = 2 also causes the stress tensor to be calculated.[71]

ISIF	calculate		degrees-of-freedom		
	forces	stress tensor	positions	cell shape	cell volume
0	yes	no	yes	no	no
1	yes	trace only	yes	no	no
2	yes	yes	yes	no	no
3	yes	yes	yes	yes	yes
4	yes	yes	yes	yes	no
5	yes	yes	no	yes	no
6	yes	yes	no	yes	yes
7	yes	yes	no	no	yes
8	yes	yes	yes	no	yes

Table 5: ISIF values, the values that are calculated and their effect on the degrees of freedom during structure relaxation.[71]

NSW

NSW sets the maximum number of ionic steps that may be taken during a calculation. If the convergence criteria have been reached before the maximum number of steps, the calculation will finish faster.[72] The value of NSW during this study changed, depending on how long the calculation was able to run on the supercomputer. If a calculation had run the specified number of steps or was externally cut off before convergence was reached, the CONTCAR file was copied to the POSCAR file and the calculation was continued.

IBRION

The IBRION tag is used to determine during the calculation in what manner the crystal structure changes. In this study, IBRION = -1 was used for static calculations as it does not allow the crystal structure to update. This was only done in combination

with NSW = 0. For relaxation calculations, IBRION = 2 was used, ensuring that the conjugate gradient algorithm was used for the structure optimization.[73]

EDIFFG

Where EDIFF defines the break in the SC-loop, EDIFFG specifies the break of the ionic relaxation loop. If a positive value is used for EDIFFG, the total energy change between two ionic steps needs to be smaller than EDIFFG. If EDIFFG is set as a negative value, the norms of all forces have to be smaller than —EDIFFG— for the relaxation to stop.[74] For this study, EDIFFG = -0.02 eV/Å was used, which means that the norms of all the forces need to be less than 0.02 eV/Å for the system to converge. This EDIFFG value was chosen to match the criteria used in the Janus-graphite relaxation calculated by Sun et al. (2021).[5]

IVDW

IVDW defines the van-der-Waals dispersion term. IVDW = 12 was used in this study, corresponding to the DFT-D3 method, which was used to express the van-der-Waals interactions.[75] Similar to the EDIFFG value, this was chosen to correspond to the study done by Sun et al. (2021).[5]

NCORE & KPAR

The NCORE and KPAR tags define how calculations are parallelised and distributed. NCORE specifies how many computing cores share calculations on an individual orbital. KPAR determines how many k-points are treated in parallel. To find the effect of these values on the speed of the calculation, speed tests were done with several values. Results can be found in Appendix B, with an optimal NCORE value of 32 and a KPAR value of 2.

ISMEAR & SIGMA

How the partial occupancies are set for each orbital is determined by ISMEAR. The width of the smearing is set by SIGMA. For the static energy and Density of States calculations, an ISMEAR value of -5 was chosen, using the Tetrahedron method with Blöchl corrections without smearing. For relaxation calculations, ISMEAR = 0 was used, producing Gaussian smearing with a width of SIGMA = 0.05 eV.[76] The SIGMA value was chosen after a convergence test, shown in Figure 15, where SIGMA values between 2 and $2 * 10^{-9}$ were tested.

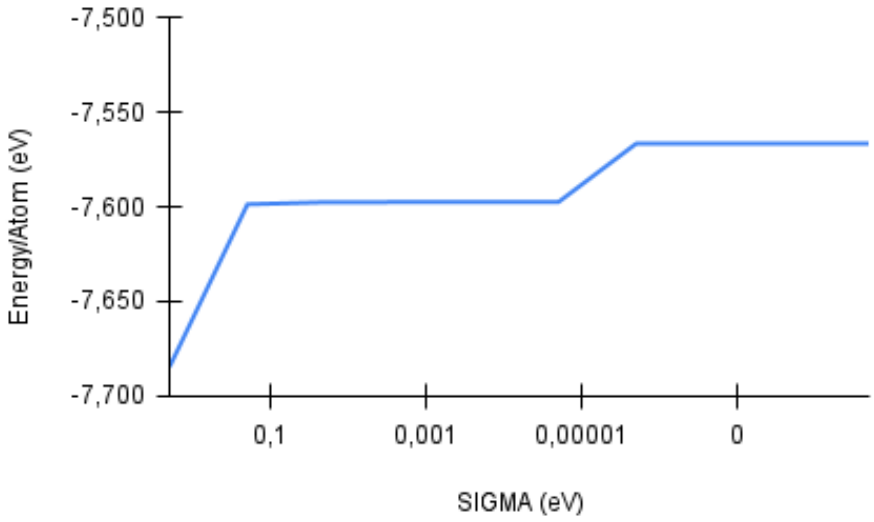

Fig. 15: Convergence test for SIGMA on a 3x3 graphene layer with a $NHCH_3$-benzene spacer, dataset can be found in Table 13 in Appendix A.

3.3.2 POSCAR

The POSCAR file contains the lattice geometry and the ionic positions of the structure. If a relaxation is run where certain atoms are not allowed to move, this is also specified in the POSCAR file with the addition of the 'selective dynamics' flag. If this flag is added to the line following the specification of the ion species, a 'T' for True or an 'F' for False may be added at the end of the coordinate lines for each coordinate. 'T' will allow the atom to move, and 'F' will lock the atom in place.[77] Appendix C contains a POSCAR file where selective dynamics is enabled.

3.3.3 POTCAR

The POTCAR consists of the pseudopotentials for the different atoms in the calculation.[78] PAW_PBE POTCAR files were used.

3.3.4 KPOINTS

The Bloch vectors, or **k**-points, used to sample the Brillouin zone are specified in the KPOINTS file. A Gamma-centred mesh was chosen, for which Equation 9 describes the **k**-points that sample the Brillouin zone.[79]

$$\mathbf{k} = \sum_{i=1}^{3} \frac{n_i + s_i}{N_i} \mathbf{b}_i \qquad \forall n_i \in [0, N_i[\tag{9}$$

To select a suitable amount of **k**-points, a convergence test was done as shown in Figure 16. The 'Number of KPOINTS' signifies the number in x and y directions. The amount of **k**-points for the x and y directions is taken as the same, and 1 **k**-point was considered for the z-direction.

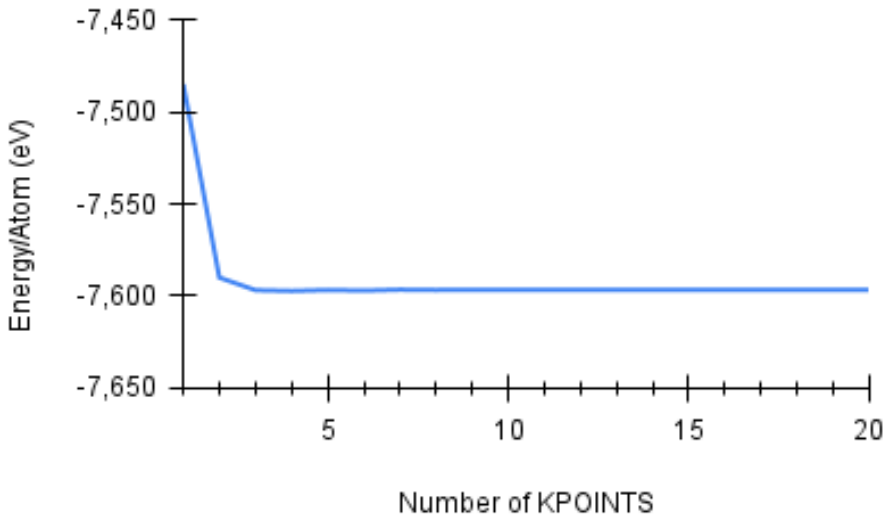

Fig. 16: Convergence test for KPOINTS on a 3x3 graphene layer with a $NHCH_3$-benzene spacer, dataset can be found in Table 14 in Appendix A.

3.4 Data Analysis

The data created during the DFT process was analysed considering charge and energy. The following sections will discuss the analysis techniques used in this study.

3.4.1 Charge

Differential Charge Density

To produce the differential charge density graphs shown in this study, the material is relaxed with an atom inserted. Then the structure with an atom, the structure without an atom, and the atom isolated are run with the tag LCHARG = .TRUE. to calculate charge densities that are stored in the CHGCAR files. VESTA is used

to subtract the charge densities as shown in Equation 10, with ρ the charge density and $\Delta\rho$ the differential charge density.

$$\Delta\rho = \rho_{total} - \rho_{structure} - \rho_{ion} \tag{10}$$

Bader Charge Analysis

To perform the Bader charge analysis, after relaxing the structure with inserted atom(s), a calculation was run with the LAECHARG = .TRUE. tag in the INCAR file. This creates the AECCAR2 file containing the self-consistent valence density. A tutorial by DB infotech was followed to obtain the ACF.dat files.[80] To calculate the charges used in the graphs of this study, Equations 11 and 12 were used.

$$Q_{corrected} = Q_{bader} - Q_{valence} \tag{11}$$

$$Q_{valence_{spacer}} = \frac{Q_{valence_H} * n_H + Q_{valence_C} * n_C + Q_{valence_N} * n_N}{n_H + n_C + n_N} \tag{12}$$

With Q the charge, n the number of atoms and $Q_{valence}$ carbon = 4, hydrogen = 1, nitrogen = 5 and sodium = 1.

3.4.2 Energy

This section details the various energies referenced in this study.

Free Energy

When 'free energy' or 'total free energy' are mentioned, this refers to the 'free energy TOTEN' that can be found at the bottom of the VASP OUTCAR file. This energy is only used when the system has fully converged.

Adsorption Energy

This study evaluates two types of adsorption energy: the adsorption of the spacer onto the graphene (Equation 13), and the average adsorption energy of the atom onto the structure (Equation 13).

$$E_{adsorption} = E_{total} - (E_{structure} + E_{spacer}) \tag{13}$$

$$E_{average\ \ adsorption} = \frac{E_{total} - (E_{structure} + nE_{atom})}{n} \tag{14}$$

with E_{total} the total free energy of the structure with inserted atom, $E_{structure}$ the total free energy of the structure without atom and E_{ion} the bulk reference energy for the used alkali-ion. For sodium, the reference energy used is -0.21995 eV, calculated from the bulk phase.[81]

Formation Energy

The formation energy describes the energy that is released or required during the chemical grafting of a benzene derivative onto a graphene surface. When the molecule attaches to the graphene, one hydrogen atom from the benzene ring is removed to form a C–C covalent bond. When two spacers attach to the graphene network at the same time, H_2 gas is formed.[82] The formation energy of this process is described by Equation 15.

$$E_{formation} = E_{total} - (E_{graphene} + E_{molecule}) + \frac{1}{2}E_{H_2} \tag{15}$$

Where E_{total} is the total free energy of the graphene with attached spacer, $E_{graphene}$ is the total free energy of the pristine graphene, and $E_{molecule}$ is the free energy of the full spacer molecule before grafting. $\frac{1}{2}E_{H_2}$ accounts for the hydrogen evolution during grafting. E_{H_2} is calculated to be -6.763 eV.[81]

4 Results & Discussion

To study the suitability of a spacer between graphene layers as part of an electrode for a sodium-ion battery, several research steps are necessary:

- Material selection
- Creation of a 3D model
- Relaxation of the structure using DFT
- Insertion of the first sodium atom
- Insertion of sodium atoms until adsorption energy becomes positive, or another goal is reached

The material must first be chosen. For this research, the electrode should specifically be suitable for a sodium-ion battery. Section 4.1 discusses the process of choosing such a material. After a material is chosen, the structure must be modelled. The 3D model is then relaxed using Density Functional Theory (DFT), which continues to optimise the structure until stress and force constraints are met. The chosen structures and their adsorption and formation energies can be found in Section 4.1.3. The structures are then loaded with atoms, as discussed in Section 4.2. There are multiple ways to approach loading a structure with atoms, and the behaviour of the first inserted atoms in combination with the structures can be used to further consider the suitability of an electrode material. Finally, in Section 4.3, all considered materials are discussed with their suitability as electrode materials in mind.

4.1 Structure Creation

4.1.1 Material Selection

Sodium ions are positively charged and are therefore attracted to materials that are negatively charged or 'activating'. Graphene itself, without added functional groups, is neutral and slightly attracts the positively charged ions. Adding negatively charged functional groups to a graphene network will allow for a more attractive negative electrode material.[83] Figure 17A shows activating functional groups, in order of their activation strength. Although the $-O^-$ substituent is categorised as the most activating, its use in a battery electrode seems unsuitable. The loading of sodium ions must be reversible for the structure to function as part of a battery, and the possible creation of an ionic bond between the oxygen and sodium atoms might hinder reversibility.[84] For this research, the three most activating structures after $-O^-$, namely

$-NR_2$, $-NH_2$ and $-OH$ were considered. For the two radicals R_2 in $-NR_2$, $-H$ and CH_3 were chosen as these are the smallest radical groups.[85]

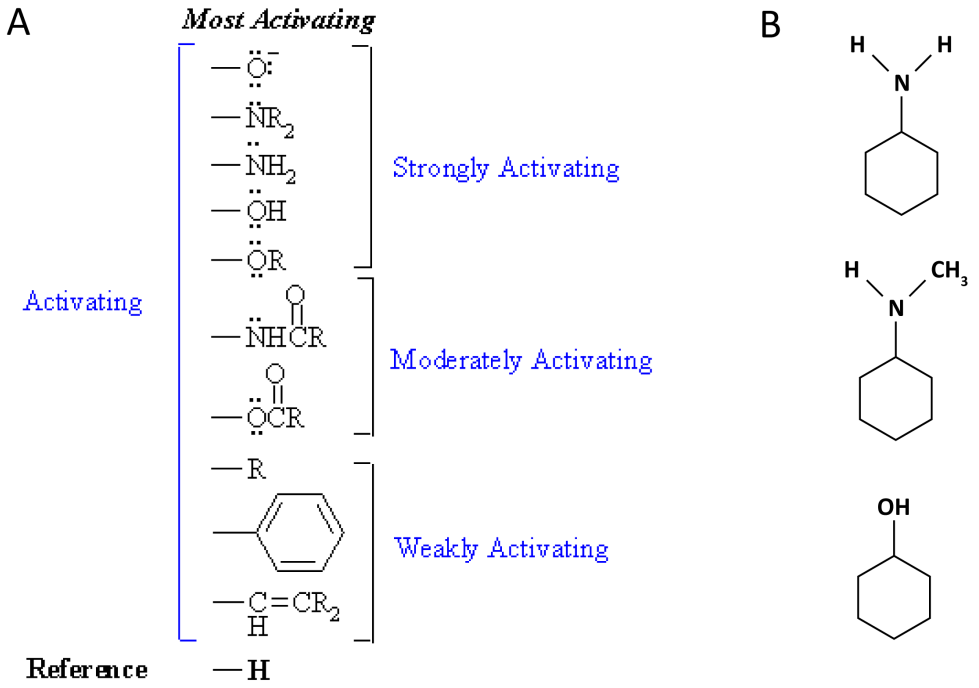

Fig. 17: A) Effect of activating substituents on the rate of reactions[86] and B) the three chosen structures, phenol, $NHCH_3$-benzene and aminobenzene, for this DFT study.

Lithium ions have a stronger attraction to neutral graphene than sodium, due to the higher electronegativity of Li^+. Compared to lithium, there is a further important difference with sodium ions, namely the size. The larger size and lower electronegativity of sodium are most likely the main contributing factors to a less successful intercalation in graphene.[4] Therefore, using an activating spacer between the graphene layers should result in a stronger attraction to the host structure, as well as creating space for the larger sodium ions. Similar to the structure created by Sun et al. (2021),[5] in this study, a benzene ring was chosen as the basis of the spacer, and the activating group was attached to the benzene ring. A simple benzene ring as the basis is a suitable choice as it can easily be grafted onto the graphene network and does not further affect the reactivity of the spacer. Thus, the effect of the functional group can be more easily studied. Figure 17B shows the three chosen spacers within this study.

4.1.2 Building the Model

To study a structure using DFT, a digital 3D model of the structure must be created. Figure 18C shows three examples of such 3D models. A graphene layer was created and relaxed, and the spacers were modelled and relaxed. Afterwards, the chosen spacer was attached to the graphene surface. However, the spacer can be attached in multiple ways.

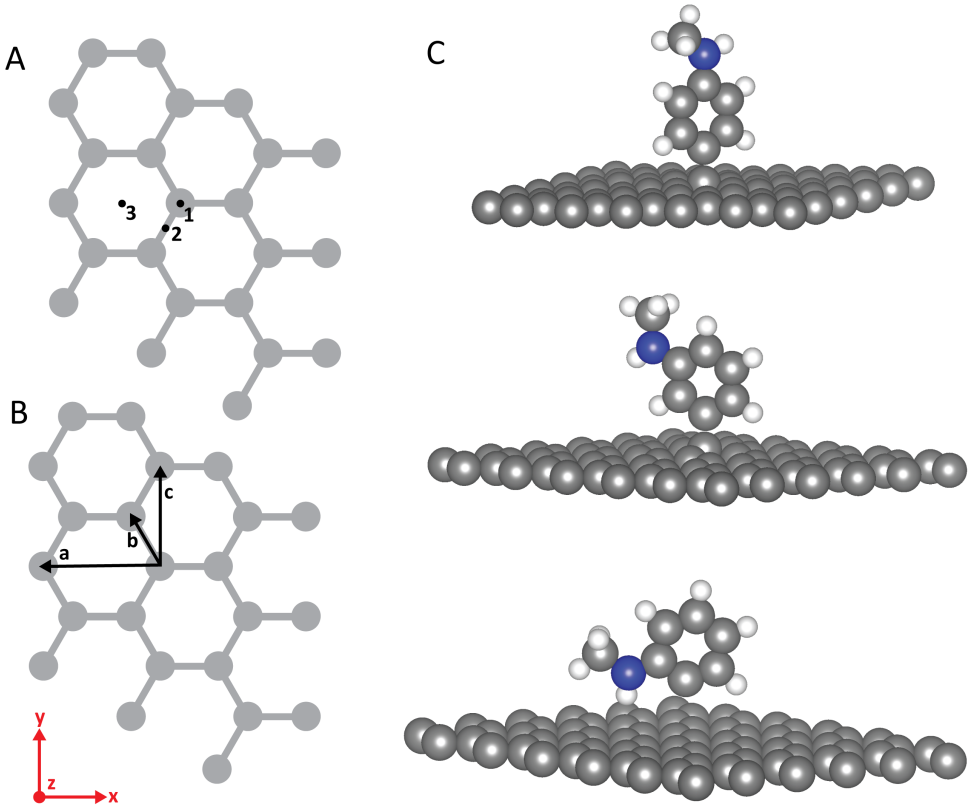

Fig. 18: A) Geometrically unique positions on the graphene surface, B) Example of possible rotations around the z-axis for the on-atom position and C) three orientations of the attached functional group to the benzene ring. Grey is carbon, blue is nitrogen, white is hydrogen, and red is sodium.

Firstly, the position of the spacer on the graphene surface has three unique positions shown in figure 18A, namely straight above one of the carbon atoms like position 1 in Figure 18A, on one of the sides of the benzene ring between two atoms, position 2 in Figure 18A or in the middle of a benzene ring as shown in position 3 in Figure 18A. Secondly, the spacer can be rotated in multiple directions depending on the position

of the spacer. An example of rotations along the z-axis for the spacer position on a carbon atom is shown in figure 18B. The spacer can further be angled along its x or y axis, leading to even more possible structures. Lastly, the orientation of the functional group on the benzene ring with regard to the graphene surface should be considered. Three orientations are possible, the para, meta and ortho orientations shown in figure 18C. After the creation of the structure, it needs to be relaxed. To relax a structure, DFT allows for the free relaxation of atoms. The single bond between the graphene and the spacer provides the structure with the ability to rotate and angle freely, eliminating the need to separately relax differently rotated structures. Similarly, the position of the spacer on the graphene network is not fixed and can move freely, thus further lowering the amount of separate relaxations necessary, as not every attachment point of the spacer to the graphene needs to be run separately. However, the orientation of the functional group cannot be changed by the relaxation process. The orientation of the functional group on the benzene does not change during DFT is most likely due to the high energy barriers that need to be overcome for that change to happen. Taking all these factors into account, three unique structures per material were considered in this study.

4.1.3 Energies

To acquire insight into the effect of the orientation of the activating group on the benzene ring, for the $-NHCH_3$ structure, the para, meta and ortho orientations were all modelled and relaxed. For the $-NH_2$ and $-OH$, only the para orientation was relaxed, to allow for a comparison between the three different activating materials. All structures were created both as 1 and 2-layer structures. The 1-layer structures consist of a graphene layer with an attached spacer, and the 2-layer structures consist of a spacer sandwiched between two graphene layers. An example of a 3D model of a 1-layer structure can be found in Figure 18C, and an example of a 2-layer structure can be found in Figure 24. Further 3D models of all structures can be found in Appendix E. The total energies, adsorption energies and formation energies of the spacers on the graphene layer can be found in Table 6. Both adsorption energies and formation energies are considered here, so they can be compared within this study. The relative adsorption and formation energies, in comparison to the lowest energy of the considered structures, can be found in Table 7 and Table 8. As adsorption energy is found often in literature, it is useful to compare it to existing research. Adsorption energy (Equation 13 in Section 3.4.2) is calculated by only considering the graphene layer and the spacer. However, the chemical process for actually making such a structure in real life involves grafting, where the spacer molecule is grafted onto the graphene surface, releasing an H^- atom. When two of the spacer molecules are grafted to the graphene, the two H^- atoms will form H_2 gas.[82] Thus the formation

energy (Equation 15 in section 3.4.2) is calculated taking this process into account. Section 3.4.2 includes more information about the calculations.

	Structure	E_{total} **(eV)**	$E_{adsorption}$ **(eV)**	$E_{formation}$ **(eV)**
1 Layer	$Para\ \ NHCH_3$	-762.399	6.050	9.542
	$Meta\ \ NHCH_3$	-762.381	6.144	9.561
	$Ortho\ \ NHCH_3$	-761.491	7.185	10.451
	$Para\ \ NH_2$	-753.711	-1.598	1.896
	$Para\ \ OH$	-747.110	-0.361	3.002
2 Layers	$Para\ \ NHCH_3$	-1440.822	1.164	1.579
	$Meta\ \ NHCH_3$	-1440.878	1.184	1.523
	$Ortho\ \ NHCH_3$	-1439.912	2.303	2.490
	$Para\ \ NH_2$	-1424.435	1.216	1.633
	$Para\ \ OH$	-1417.809	2.477	2.762

Table 6: Total, adsorption and formation energies of the single and double layer relaxed structures. Para NH_2 has the lowest energies for the single-layer structures. The double-layered structures have very similar energies for para $NHCH_3$, meta $NHCH_3$ and para NH_2.

Examining the adsorption and formation energies, the meta and para orientations of $NHCH_3$ do not have a large difference in energy. However, the ortho orientation is different. Both the adsorption and the formation energies agree on the para-orientation being the most suitable of the $-NHCH_3$ options. The relative energies of the para, meta and ortho-$NHCH_3$ structures are shown in Table 7. The 2-layer $-NHCH_3$ structures all have significantly lower adsorption and formation energies, indicating that they would be easier to form. Of the different single-layer materials, $-NH_2$ has the lowest adsorption and formation energies, suggesting it would be most suitable of the structures to be used as a spacer. However, when considering the double-layered structures as well, the adsorption energies of the para and meta $-NHCH_3$ are lower. The formation energies for the 2-layer structures show that to form either of para$-NHCH_3$, meta$-NHCH_3$ or para$-NH_2$ structures, the energies would be very similar (Table 8). Thus, $-NH_2$ would still be a great candidate.

	1 layer		*2 layer*	
	Relative Adsorption Energy (eV)	**Relative Formation Energy (eV)**	**Relative Adsorption Energy (eV)**	**Relative Formation Energy (eV)**
Para-$NHCH_3$	0	0	0.019	0.056
Meta-$NHCH_3$	0.094	0.018	0	0
Ortho-$NHCH_3$	1.136	0.908	1.119	0.967

Table 7: Relative adsorption and formation energies for the para, meta and ortho orientations of $NHCH_3$-benzene for 1 and 2 layers as compared to the lowest energy.

	1 layer		*2 layer*	
	Relative Adsorption Energy (eV)	**Relative Formation Energy (eV)**	**Relative Adsorption Energy (eV)**	**Relative Formation Energy (eV)**
Para-$NHCH_3$	7.648	7.647	0	0
Para-NH_2	0	0	0.052	0.053
Para-OH	1.237	1.106	1.313	1.183

Table 8: Relative adsorption and formation energies for para-$NHCH_3$, Para-NH_2 and Para-OH for 1 and 2 layers as compared to the lowest energy.

A positive adsorption or formation energy of a structure implies an endoergic process, where it is needed to add energy to create the structure. Consequently, such a structure would not be able to form spontaneously.[87] Almost all of the adsorption and formation energies in Table 6 are positive, except for single layer $-NH_2$ and OH^-. At first glance, this means that nearly all structures considered would not be very suitable to form. However, the calculations used here are both a simplification of reality as well as beholden to the exact input values that are used for the DFT calculations. For example, Sun et al. formed the $-NH_2$ structure, meaning it is possible. However, they did use a different process than considered here for the formation, where they grafted on a molecule which released N_2 instead of H_2 gas. Thus, as is often the case with DFT studies, the calculated energy values are more meaningful when compared within the study.[87] Where the structure with the lowest adsorption and formation energies, be it positive or negative, is simply more likely to form than the other structures considered.

4.2 Ion loading

4.2.1 Functional Group Orientation

As mentioned in the previous section, the three possible orientations for a benzene derivative are para, meta and ortho. The adsorption energies of the spacer onto the graphene layer shown in Table 6, indicate that there is very little difference between para and meta, while the ortho structure has a higher adsorption energy. Figure 19 shows the differential charge density of the structures with the three different orientations when one atom is loaded into the structure. Section 3.4.1 specifies the calculation of the charge density. For all three structures, the relaxed position of the atom is at the graphene surface, close to the spacer. For the para and meta orientation, the atom sits directly next to the benzene ring of the spacer, while the atom in the ortho structure located itself closer to the nitrogen atom. With the nitrogen atom of the ortho orientation closer to the graphene surface, the atom can easily move closer, without an energy penalty from moving further away from the graphene surface. The functional group $NHCH_3$ in the para structure does not appear to interact with the atom at all, as no charge depletion or charge accumulation is visible on the functional group when observing the charge density in Figure 19. The meta and ortho structures do show some interaction of the nitrogen atom.

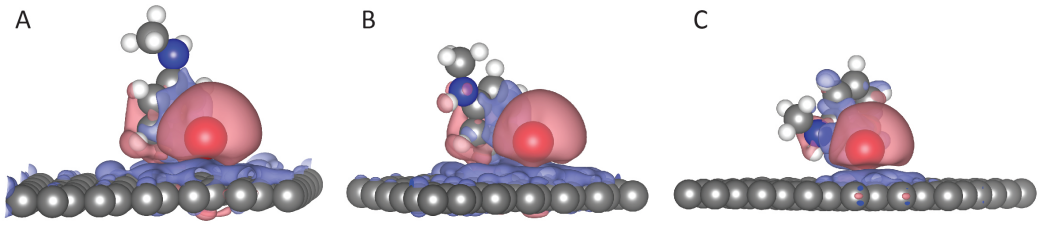

Fig. 19: 3D figures of the differential charge density of the $NHCH_3$ structure in A) Para, B) Meta and C) Ortho orientations. Charge accumulation is shown in blue, and charge depletion in red.

Although there are slight differences visible in the charge density shown in Figure 19, there is hardly any significant difference to be found in the adsorption energies of the atoms. Figure 20 shows these adsorption energies of the three structures for each added atom. Ortho-$NHCH_3$ has a slightly lower adsorption energy, and the para and meta structures are nearly identical. The slightly lower adsorption energy for ortho could be explained by the functional group being oriented closer to the graphene surface, as the first atom can coordinate itself both close to the functional group and to the graphene surface. From the first to the sixth atom, each step was

relaxed individually. To understand the behaviour at loading with more atoms, the extra six atoms were added at once. However, the adsorption energy of 12 atoms is very similar for the three structures. Therefore, the behaviour of the materials when loaded with atoms does not indicate one optimal orientation.

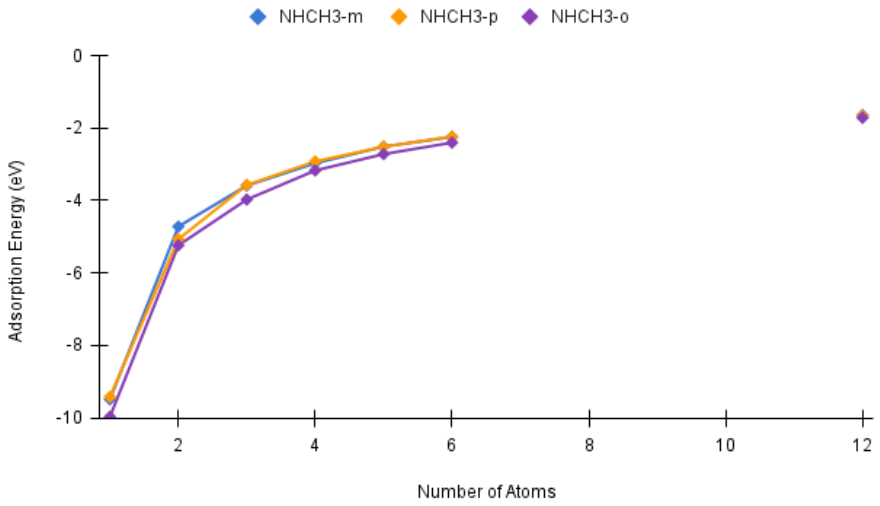

Fig. 20: Adsorption Energy of the Para, Meta and Ortho orientations of the $NHCH_3$ structure for 1 to 6 atoms and 12 atoms.

4.2.2 Comparing Sodium Atom Loading Methods

Considering the effect of loading atoms to evaluate the suitability of a structure using adsorption energy and charge analysis is a common approach in literature.[5–7] This is often carried out using a one or two-layer structure and the atoms are loaded step by step. However, information on the exact input values is often shared only in part, with a figure of the 3D structure or atom placement shared but not the exact input coordinates, or only some of the relevant INCAR tags specified.

First Sodium Atom

The research done by Sun et al. (2021)[5] was used here to compare strategies for calculating and evaluating loading of the first atom. A more detailed analysis of their research can be found in Section 2.3.1. The structure used by Sun et al. consists of one spacer between two 6x6 graphene layers. The spacer on a single graphene layer was relaxed using DFT. To evaluate the optimal layer distance, several distances were tested, and the configuration with the lowest total energy was selected. The spacer consists of a benzene ring with a NH_2 functional group located at the para

position. The input values specified in the paper are shown in Table 9. To evaluate the behaviour of the first atom, they inserted the atom at several positions and statically calculated the adsorption energies to find the most stable location.[5] Figure 21A shows their optimal position of the atom and differential charge density caused by the insertion of the atom, and Figure 21C shows the examined positions with their relative adsorption energies.

	Sun et al.	**This Study**
Layer Distance (Å)	10	10.09
Maximum Force (eV/Å)	0.02	0.02
Cutoff Energy (eV)	500	550
Exchange-Correlation Functional	PBE-D3	PBE-D3

Table 9: Input values specified in Sun et al.,[5] and the respective values used in the comparison study done in this research

To compare, the same spacer was used here, between two graphene layers of 6x6 atoms. However, to find the optimal version of the structure, the full structure was relaxed using DFT. The optimal layer distance is very similar, with a value of 10.09 Å instead of 10 Å. The same maximum force and a slightly higher cut-off energy were used, as can be seen in Table 9. Instead of static insertion of the sodium, the atom was placed in the structure and allowed to move freely to discover the optimal position. In contrast to Sun et al., the atom relaxed near the bottom of the spacer instead of at the nitrogen atom. Figure 21B shows the differential charge density of the adsorbed atom. To verify that the atom did not end up in a local minimum, static insertion at the same locations as in the Sun et al. paper was done as well, with a similar result to the free relaxation (Figure 21D). Figure 21C and D have adsorption energies noted in the corner of the figures, relative to the lowest energy in their study. So for the Sun et al. figures, the energies are relative to the energy of the atom coordinated at the $-NH_2$ group, and for the figures of this study, the energies are relative to the atom coordinated at the benzene ring. These static calculations further establish that the optimal atom position found in the free relaxation was indeed not a local minimum when comparing these four positions. However, when taking a very close look at the exact position of the atom in the top left image of Figure 21D, and comparing it to the top left image in Figure 21C, the position of the atom might be slightly further away from the $-NH_2$ group and closer to the upper graphene layer. This may have influenced the calculated energy, and could at least explain why the $-NH_2$ structure corresponds to the highest energy configuration in this study.

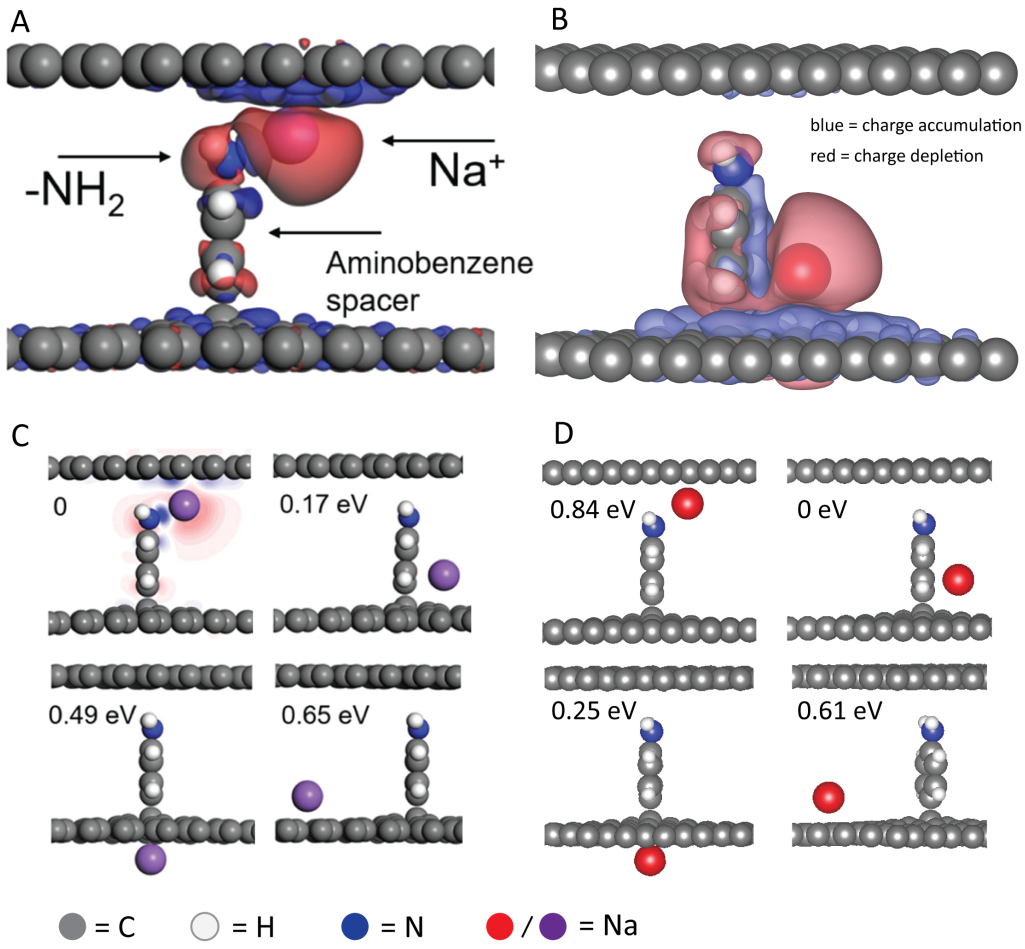

Fig. 21: Comparison between DFT study by Sun et al.[5] and DFT study in this thesis by differential charge analysis of A) Janus-graphene[5] and B) freely relaxed atom in the comparison structure. And static energy calculations of C) Janus-graphene[5] and D) the comparison structure with their relative adsorption energies.

Although the atom position was not identical, the free relaxation also placed the atom in front of the benzene ring, which shows that there may have been another relevant change in the inputs, structure or atom loading process. Although the inputs given by Sun et al. were used or were very similar, many key parameters were not specified, such as the EDIFF, ISMEAR and SIGMA values, and can thus not be compared. Furthermore, less complete relaxation of the structure was done by Sun et al., with the bottom layer and spacer fully relaxed, but the top graphene layer only added at a distance chosen by running several static calculations. Similarly, the atoms were placed and the adsorption energy calculated, without relaxation of the structure with

atom. Although the layer distance itself is very similar, it is possible that in the free relaxation process done as a comparison, the spacer was also free to acquire small changes. As in this study the complete structure was allowed to relax fully, giving all atoms the opportunity to reach their optimal position. Visually, the structures seem very similar, but unless exact coordinates are available (such as a POSCAR file), this is also something that is difficult to establish. Lastly, as the static loading of the atom was also tried here, the process should thus have been very similar.

Further Loading

As seen in the previous section, seemingly small changes in input values can lead to significantly different behaviour of the system. Aside from the input values for DFT, the starting position can potentially also have an effect due to a local minimum being found. The process most often found in literature is a structure that is loaded step by step. For each step, multiple positions are tried and their corresponding energies are statically calculated.[6,7] This is understandable, as calculation times for static energy calculations are notably lower. Especially for relatively large systems for DFT, as considered here. Trying multiple positions can also prevent accidentally finding a local minimum. However, the exact location the atom might occupy would have to be assumed correctly, considering radii and all unique positions an atom could absorb at. Each step would save in calculation time, but would cost more time to prepare during the study, as multiple locations have to be modelled per step. To evaluate different options for loading a structure, three different methods of loading the structure with atoms were tried within this study:

1. The host material was loaded with the atoms in steps, with one atom added to a fixed structure using selective dynamics. The equilibrium position of the atom was approximated using DFT. Next, this atom was fixed as well before a new atom was added, and so on. This was done up to and including 18 atoms.

2. The fixed structure was loaded with respectively 6, 12, or 18 atoms at once, using starting positions similar to (the first of) the optimised positions of method 1. All atoms could freely move.

3. Similar to method 2, the fixed structure was loaded with 6, 12, or 18 atoms at once. However, the starting positions of the atoms were set into a grid formation around the spacer (The starting formation of method 3 can be observed from Figure 23).

	E_{6atoms} (eV)	$E_{12atoms}$ (eV)	$E_{18atoms}$ (eV)
Method 1	-777.178	-783.713	-791.892
Method 2	-777.631	-784.750	-793.544
Method 3	-777.534	-785.564	-793.579

Table 10: Total free energy of the $NHCH_3$ system with 6, 12 and 18 atoms calculated via three different methods

Method 1 was designed to require less input during the study, as each step only involves one calculation. Of course, the risk of local minima is higher, as is the computing time per step. Fixing all atoms except the newest one was done in an effort to still minimise the computing time, with the risk of an overall higher adsorption energy. Since the other atoms cannot move, no further relaxation of all the atoms as a whole can happen. Table 10 shows the optimised adsorption energies for the three methods for 6, 12 and 18 atoms. It is indeed visible that the adsorption energies for method 1 are higher than for the other two methods. Method 2 was designed to be used in combination with either method 1 or the original method now often used in other studies. When data is gathered from the interaction with the first few atoms, the most stable positions are used, and if needed, more atoms are added to dynamically calculate the energy of the structure. This way, larger amounts of atoms can be calculated to provide insight into the maximum sodium atom packing, while still avoiding local minima for the strongest interacting atoms.

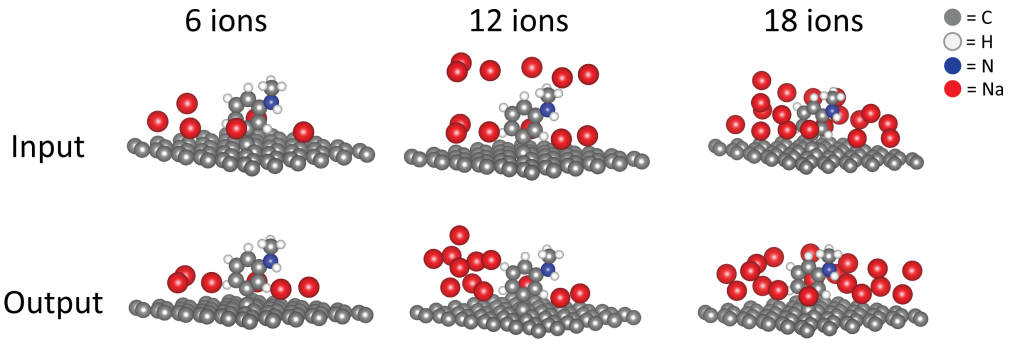

Fig. 22: Starting and ending positions of 6, 12 and 18 atoms, for method 2.

Figure 22 shows the starting and optimised positions for the atoms when method 2 is used. The 6-atom output shows that the atoms did move around, but there are no great changes. The atom at the back of the spacer is the first atom to have been

placed, and it seems to stay in the exact same position. In the 12 and 18 atoms, this atom can also be seen in a similar position. The output of 12 atoms appears to show something of a bulk sodium structure forming, which might possibly have been caused by the placement of the extra atoms high above the benzene layer, from 6 to 12 atoms. The 18-atom structure is complicated to analyse as there are so many atoms, but it does seem to show that here, in contrast to the 6-atom output, the atoms all stick closer to the graphene surface. Method 3 was conceived with the idea of some level of automation in mind. If one wishes to observe the viability of multiple structures quickly, the one-by-one placement of the atoms seems cumbersome. Instead, here an approach was tried where the starting positions of the atoms were coordinated in a grid-like formation, visible in the upper row of Figure 23, to observe if this would be a viable strategy. The total free energies of method 3 are surprisingly similar to method 2, as can be seen in Table 10. Looking at Figure 23, similar to the tests of method 2, there appears to be an atom orienting itself next to the benzene ring, which would correspond with one of the preferred positions for the atom (Figure 19 shows the preferred atom position). At the back of the 12-ion output, the atoms are stacking themselves in an alternating configuration, possibly indicating the formation of bulk sodium. The 18-atom structure has atoms orienting themselves at the front and back of the benzene ring. The atoms are spread more in height, showing a possible effect of the height of the starting position. Especially when compared with the 18-ion structure of Figure 22 where the starting position of the atom is close to the graphene surface, and the relaxed position is also close to the graphene surface.

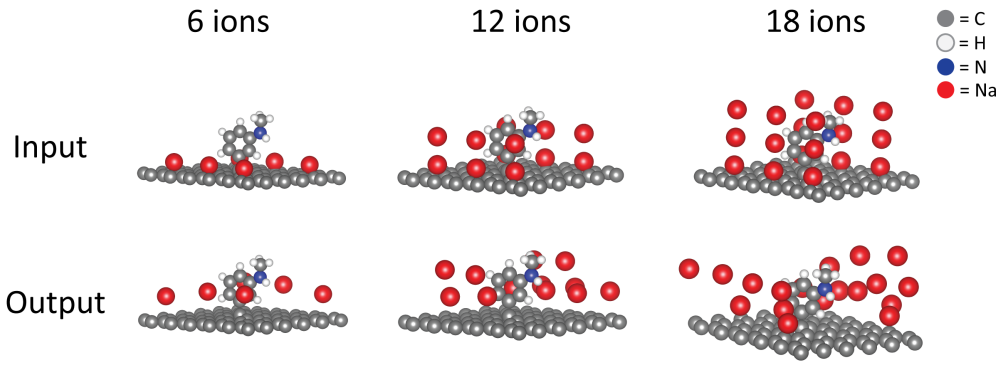

Fig. 23: Starting and ending positions of 6, 12 and 18 atoms, for method 3.

The starting height of the atoms seems to have a significant impact on the final positions, both in methods 2 and 3. In method 3, the used grid was spaced further apart in height, but that could be easily remedied if they were placed closer together in height, or if there were more atoms per grid layer. Similarly, the added atoms in the

12-ion setup for method 2 must be placed lower, most likely thereby avoiding a bulk structure forming in the manner observed here. With both methods with all amounts of atoms, one or two of the atoms positioned themselves next to the benzene ring of the spacer. The effect of the starting positions on the graphene surface does not seem to be of much relevance, except for the starting height. Methods 2 and 3 do seem like a good option for quickly estimating the effect of a large number of atoms in a system, even while still using the lowest energy positions. However, they would need to be used in combination with relaxing the first few atoms separately to understand what is happening during sodium atom loading. Furthermore, in this study, a single spacer is used on a large slab of graphene, which means there is relatively little interaction with the spacer and a lot of space to move around. Thus, it is uncertain if one of these methods will still work well in a more crowded structure with multiple spacers.

1-Layer vs 2-Layer Structure

A further aspect to consider, aside from the staring positions of the atoms, is whether a single-layer or double-layer structure is used. When observing the behaviour of sodium atom insertion, having a single-layer structure might disregard the interactions that the atom could have with a layer above. Especially since in an actual electrode material, the functionalized graphene would be stacked in layers.

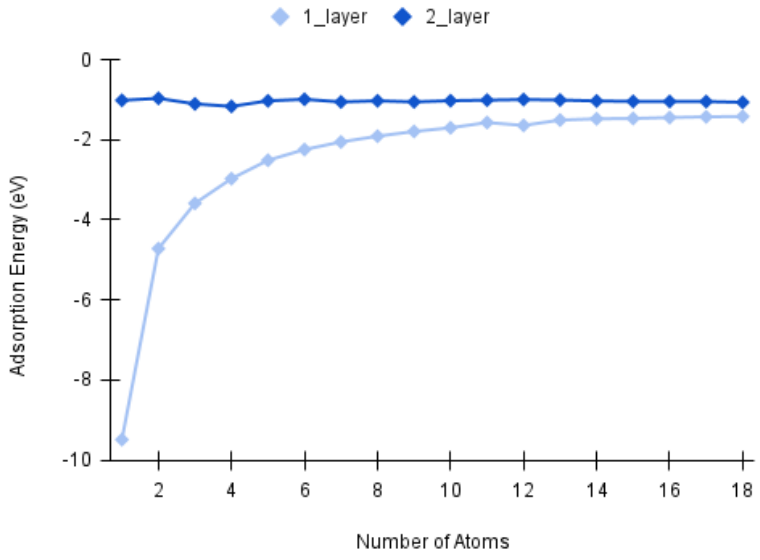

Fig. 24: Adsorption Energy of 1-layer and 2-layer of the meta-$NHCH_3$ material for each added atom.

To gain further insight into the difference in behaviour between a single and double layer structure, the Bader charges can be calculated and evaluated. The method of calculation for the Bader charges is elucidated in Section 3.4.1. Figure 25 and Figure 26 show the Bader charge, corrected for the valence charge, of the atoms, graphene and the spacer separately to observe what happens in the structure. The Bader charge of the 1-layer structure in Figure 25 shows a notable change for the atoms and the spacer at around 8 atoms, which corroborates the behaviour in Figure 24. The Bader charge goes from near zero for the first 8 atoms to 0.63 e^-, after which the Bader charge gradually moves towards 0 again. The spacer makes an opposite movement, where the 8th inserted atom causes the Bader charge to sharply jump to -0.44 e^-. The Bader charge starting around 0 and suddenly changing at 8 atoms might be attributed to the atoms settling on the graphene surface without any effect on the charges of the graphene, spacer and atoms. The spacer and atoms both react oppositely regarding Bader charges, indicating an interaction between the spacer and the atoms. It is possible that the graphene surface was fully occupied after 7-8 atoms, which explains the sudden shift to interaction with the spacer. This explanation is supported by the atom locations found in appendix E. The 7th atom coordinates itself above other sodium atoms, but not close to the spacer. The 8th atom also coordinates itself above the other sodium atoms, but close to the $-NH_2$ functional group. The 9th sodium atom coordinates itself at the back of the spacer.

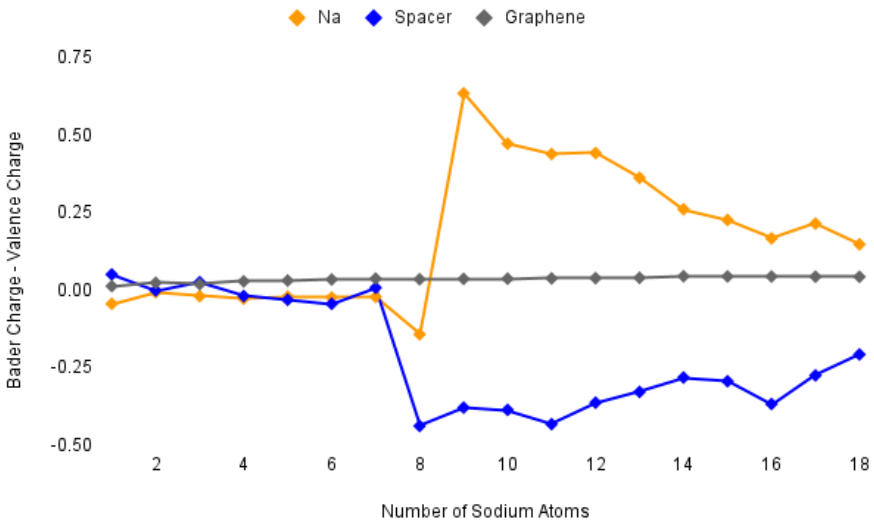

Fig. 25: Bader analysis of single-layer graphene with a $NHCH_3$ spacer. Data can be found in Appendix F.

Observing Figure 26 for the 2-layer structure shows a very different distribution of the Bader charge. Both Graphene layers and the spacer do not have any interaction with the sodium atoms. The sodium atom starts with -1 e^- and slowly moves up to -0.29 e^-. Appendix F contains the 3D images for every added atom. The atoms start further away from the spacer than with the single-layer structure, and start relaxing closer to the spacer when more atoms are added. There is a clear difference in the behaviour of the inserted atoms between the 1-layer and 2-layer structures. In the case of a single spacer with a large graphene surface, it appears to be necessary to also take into account the second layer, as the behaviour of the atoms can change. However, if instead of a single spacer, multiple spacers were used, the effect of a large surface of graphene would disappear. Thus, the effect of a second layer added should be tested for a multiple spacer structure as well.

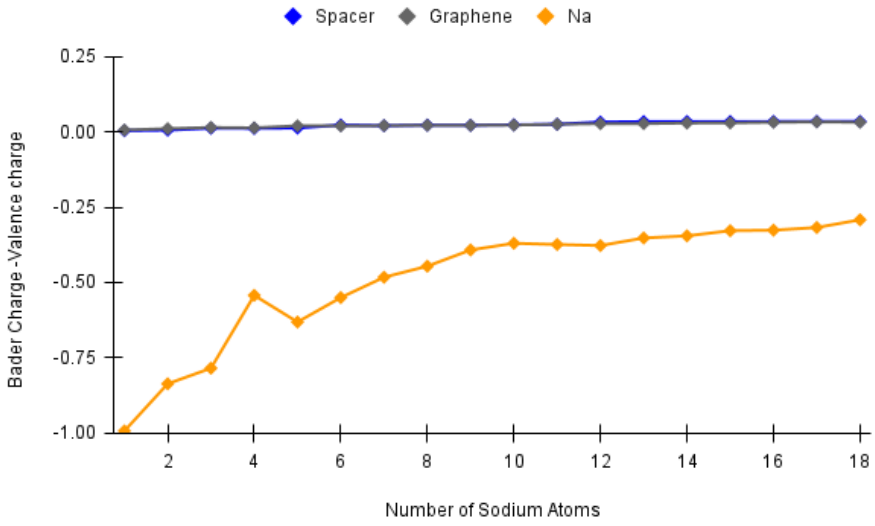

Fig. 26: Bader analysis the $NHCH_3$ spacer between two layers of graphene. Data can be found in Appendix F.

4.3 Comparing $-NHCH_3$, NH_2 and $-OH$ structures

Figure 27 shows the adsorption energies per added atom for all of the previously mentioned spacers, between two graphene layers. The atom loading occurs similarly for most structures except meta-$NHCH_3$, where the first atoms do not exhibit as low an adsorption energy. Similar to what was seen in the previous section, the adsorption energy for all structures seems to stabilise between -1.5 eV and -1 eV.

Since these structures all consist of a single spacer on a large graphene layer, the atoms can easily settle on the graphene surface or interact with each other without an energy penalty from other nearby spacers. To evaluate this, Figure 27 shows the adsorption energies of 6 and 12 atoms on a single graphene layer without a spacer, as well as 6 atoms inserted between two graphene sheets without a spacer. The 2-layer graphene clearly shows the expected behaviour,,[4] where sodium insertion is difficult because the graphene layers are too close together for the large sodium to fit comfortably. Comparing the empty 2-layer graphene with the spacer structures shows an improvement in adsorption energy of the atoms for the structures with spacers, demonstrating that using a spacer can indeed be an effective strategy to improve insertion of larger atoms.

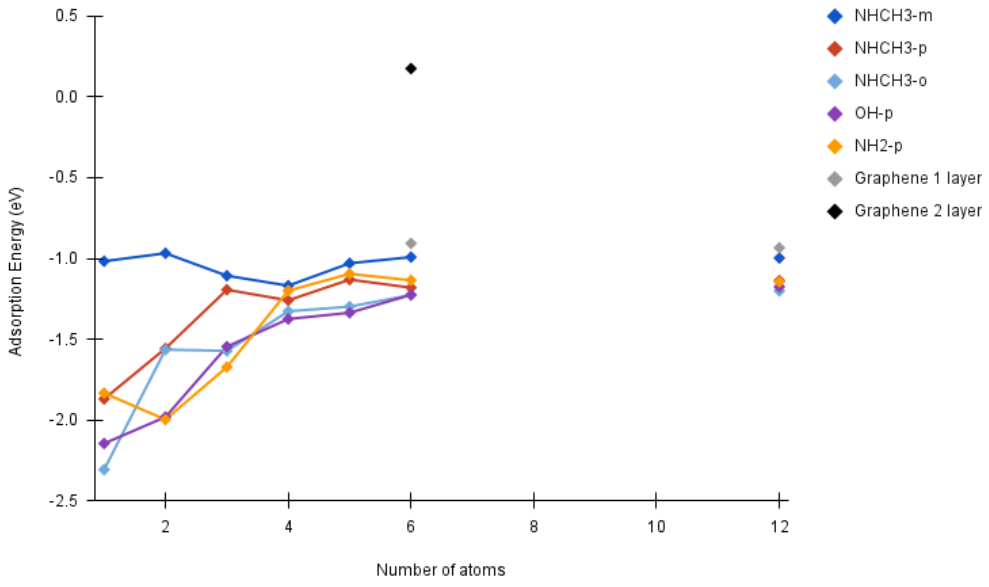

Fig. 27: Adsorption energy of 2-layer $NHCH_3$-benzene in meta, para and ortho orientations and 2-layer phenol ($-OH$) and aminobenzene ($-NH_2$) in para orientations. In grey, a single layer and a double layer of pristine graphene of the same size are added as a reference.

The spacer structure moves the graphene layers further apart, lowering the graphene-graphene interactions, indicating that, in addition to comparing the structures with the double-layer graphene, single-layer graphene might also give insight. The adsorption energies of the 6 atoms and 12 atoms on graphene are almost the same, at around -0.9 eV. With adsorption energies of the para-$NHCH_3$ stabilising at -1.14 eV, meta-$NHCH_3$ at -1 eV, ortho-$NHCH_3$ at -1.20 eV, $-NH_2$ at -1.14 eV, and $-OH$ at -1.18 eV, the adsorption energy on pristine graphene is slightly higher than the

adsorption energies of the spacer structures. All of the structures exhibit similar behaviour, where the adsorption energy of 6 atoms is almost the same as the adsorption energy of 12 atoms. Additionally, for some of the structures, the adsorption energy of 18 atoms was calculated and was found to also be very close to the 6-atom and 12-atom adsorption energies. All the calculated adsorption energies can be found in Appendix D. Since the stabilising behaviour where the adsorption energies stay nearly the same can be seen in all structures, including the graphene layer without a spacer, the graphene layer is likely the main contributor the this behaviour. Consequently, if more spacers were to be placed on the graphene layer, this behaviour would change. The adsorption energies would most likely also become positive, as there would be no exposed graphene network to settle on, or space for the sodium to form a bulk-like structure.

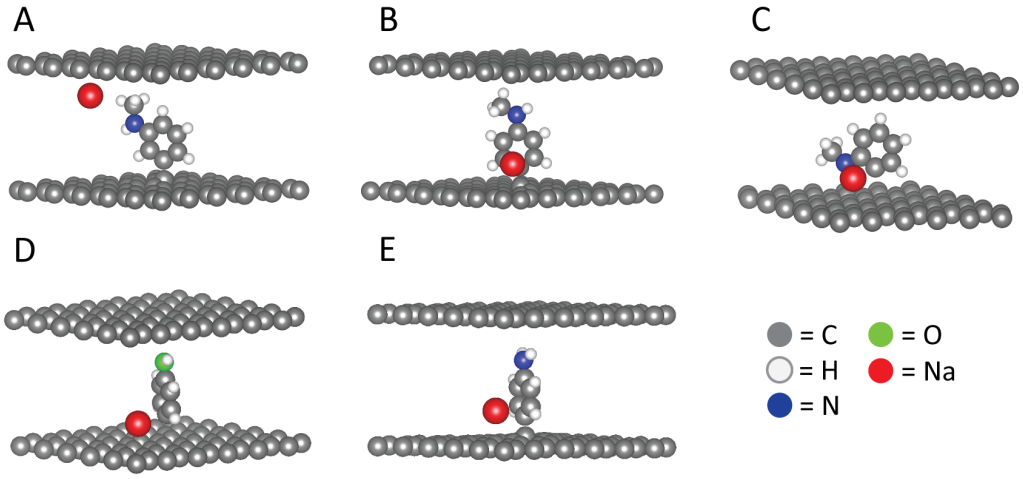

Fig. 28: First adsorption location of A) meta-$NHCH_3$, B) para-$NHCH_3$ C) ortho-$NHCH_3$, D) para$-OH$ and E) para$-NH_2$. All structures have a preferred atom position close to the benzene ring, except for meta-$NHCH_3$, where the atom is located close to the functional group at the top graphene layer.

The most stable configuration of the first inserted atom is shown for all the structures in Figure 28. The preferred adsorption positions of all structures except meta-$NHCH_3$ are near the benzene spacer on the bottom graphene layer. Meta-$NHCH_3$, however, has a preferred first atom position near the -$NHCH_3$ group, close to the top of the graphene layer. This can explain the deviant behaviour of meta-$NHCH_3$ seen in Figure 27. The adsorption energy for the first of the inserted atoms is already around the -1 eV that the atoms for this structure end up stabilising at. It is very possible that for this structure, the atom found a lower local minimum. Appendix E shows the positions of the atoms for every added atom for the meta structure.

The first and second inserted atoms find their relaxed position further away from the spacer, but the third and fourth atoms coordinate themselves close to the spacer. This behaviour matches with the adsorption energies observed from Figure 27 where there is a dip in energy at the third and fourth inserted atoms.

5 Conclusion

The main research objective of this study was to determine the viability of $NHCH_3$-Benzene, Aminobenzene and Phenol as spacers between graphene layers. All structures were found to be improvements on graphene layers with no spacers. When considering the adsorption and formation energies of the spacer attaching to the graphene layer(s), the para$-NH_2$ spacer is the best choice of the materials tested in this study, as it has the lowest single-layer energies, as well as having one of the lowest energies of the double-layer structures. A further benefit is that, as opposed to the $-NHCH_3$ structure, the $-NH_2$ structure can easily be produced, as shown in the paper by Sun et al. (2021)[5] where they created and stacked graphene with aminobenzene spacers. The structures discussed in this work were then loaded with atoms, first with a single atom. Although there were slight differences, such as a preferred orientation of the first atom at the $-NHCH_3$ functional group for the meta-$NHCH_3$ spacer, the structures behaved very similarly with a preferred atom position near the benzene ring of the spacer, close to the bottom of the graphene network. However, the deviant behaviour of the meta-$NHCH_3$ might well be explained by the atom settling in a local minimum.

Aside from studying the suitability of the materials for use as electrode materials, the secondary objective was to investigate the importance of the experimental setup of the Density Functional (DFT) study on inserted atom behaviour and adsorption energies. To study the effect of changes in the trials, first, the starting positions of the sodium atoms before relaxation were manipulated. To evaluate the global behaviour of a single-layer spacer structure when loaded with a large amount of atoms, a grid-like starting placement was found to be a valid strategy, as long as the height of the atoms from the graphene surface is constrained. Although the most stable position was seen in each of these relaxations from grid starting positions, to really get an understanding of what the first preferred positions of the atoms are, the starting atoms should still be relaxed separately. Additionally, a comparison between the same structure on one graphene layer and between two graphene layers was performed, finding that a second layer can have an effect on the found adsorption energies of added atoms. Lastly, the repeatability of the study by Sun et al. (2021)[5] was tested. To improve repeatability of DFT research, more specific inputs such as full INCAR and POSCAR files should be shared. While figures of the 3D-model are often included in papers, coordinates are usually not included. As seen in Section 4.2.2, with hardly any change from the given values in the compared paper, a different most stable position was identified

within this study. However, further comparison was not possible due to the absence of additional DFT data, such as input values for EDIFF, ISMEAR and SIGMA, or exact coordinates for the spacer-graphene structure or inserted atoms. While this is just one example, it reflects a broader trend where only a few input values are often provided, despite the fact that they can significantly influence the results.

6 Recommendations

This study focused on graphene layers with a single spacer to observe the effect of small changes to the spacer material. A logical next step would be to more closely simulate a real electrode material. Instead of a single spacer, the material can be loaded with multiple spacers. An endeavour to outline a suggestion for the entire process for computational validation of a spacer on graphene as an electrode material in an alkali-ion battery is made with the following 10 steps:

1. Material selection and creation of a 3D model.

   After choosing the material, the optimal attachment to the graphene layer is investigated. The graphene layer is then loaded by the maximum number of spacers, where the energy stays exothermic.

2. Relaxation of the structure using Density Functional Theory (DFT).

3. Calculation of formation energy.

   Formation energies are important to calculate as they represent the possibility of creating the structure in reality.

4. Insertion of the first atom.

   The placement of the first atom will indicate the most stable positions for insertion. Even using a DFT relaxation where the inserted atoms can freely relax, in a tight-packed structure trying out various starting positions for the atoms is recommended.

5. Insertion and relaxation of atoms until the adsorption energy becomes positive, or another goal is reached.

   Multiple different alkali-elements can be tried to observe the difference in insertion behaviour.

6. Calculation of adsorption energies of the inserted atoms, and the Bader charges of the system.

7. Molecular Dynamics (MD) simulation to observe the diffusion pathways of the ions through the structure.

8. Test the thermal stability by running a MD simulation at ambient temperature.

9. Calculation of theoretical energy density.

The theoretical energy density is one of the values that can most easily be compared with existing batteries and other battery studies, as it gives an estimate of how much energy the battery can store.

10. Calculation of open circuit voltage.

    The open circuit voltage signifies the ease of charging and discharging the electrode, which is essential to a battery.

The experiments done in this study go up to point 6 of the above list, but with a single spacer. It was observed that the graphene-phenol structure was the most interesting candidate of the tested structures, but further research is essential. Loading the graphene layer with multiple phenol spacers and following the steps above would be a great start in validating the structure for use as an electrode material. Points 9 and 10 of the list above will allow theoretical computational research to be connected to the practical application of the electrode in a battery. A combination of Density Functional Theory and Molecular Dynamics is useful for thermodynamics and kinetics. Combining these research steps further with a technique like Machine Learning (ML) might lead to interesting insights. A model can be trained on existing calculations to predict possible materials to use as spacers, or even full electrode materials. However, a large database is needed to train a model. To achieve this, many calculations need to be run or shared within the research community. A platform for sharing DFT data behind experiments would be beneficial. There are already some examples, such as JARVIS-DFT.[88] If use of such a platform were more widespread, this could serve as a database to train models on, in addition to improving repeatability of experiments. Furthermore, having a central database will allow for the continuation of research without repeating computationally expensive experiments.

7 Acknowledgements

I would like to thank my supervisors, Dr. Poulumi Dey and Dr. Nabil Khossossi, for introducing me to the fascinating field of Density Functional Theory and fundamental battery research. Their endless patience and wonderful attitudes were essential in completing my thesis. I would further like to thank my friends Freek and Robert, who went through a large part of the thesis process at the same time and made the hours of reading literature and writing enjoyable. My other study friends, Aditya, Laura and Elena were wonderful in their constant support and enjoyable moments throughout my studies. Special thanks go out to my partner, Chris, who supported me throughout the whole process, and my mother, who regularly scheduled moments to work together and helped me through some of the tough spots during my thesis process.

References

[1] International Energy Agency. Global EV outlook 2025, 2025. Online; 31-07-2025.

[2] Mads Lykke Andersen. The crucial role of battery storage in energy grids, 2025. Online; 31-07-2025.

[3] TRENDS research and advisory. Japan's shift from lithium to sodium batteries: A strategic pivot in energy storage and supply chain resilience, 2025. Online; 31-07-2025.

[4] M. R. Palacín. Recent advances in rechargeable battery materials: a chemist's perspective. *Chemical Society Reviews*, 38:2565, 2009.

[5] Jinhua Sun, Matthew Sadd, Philip Edenborg, Henrik Grönbeck, Peter H. Thiesen, Zhenyuan Xia, Vanesa Quintano, Ren Qiu, Aleksandar Matic, and Vincenzo Palermo. Real-time imaging of na^+ reversible intercalation in "janus" graphene stacks for battery applications. *Science Advances*, 7(22), 2021.

[6] Hristo G. Rasheev, Rafael B. Araujo, Alia Tadjer, and Patrik Johansson. Fundamental promise of anthraquinone functionalized graphene based next generation battery electrodes: a dft study. *J. Mater. Chem. A*, 8:14152–14161, 2020.

[7] F. Peymanirad, R. Majidi, S. I. Vishkayi, and H. R. Soleimani. Density functional theory study of molecular pillared graphene for high-performance sodium-ion batteries. *Applied Surface Science*, 669:160502, 2024.

[8] Claude Delmas. Sodium and sodium-ion batteries: 50 years of research. *Advanced Energy Materials*, 8:1703137, 02 2018.

[9] Odne Stokke Burheim. Chapter 7 - secondary batteries. In Odne Stokke Burheim, editor, *Engineering Energy Storage*, pages 111–145. Academic Press, 2017.

[10] John B. Goodenough. Evolution of strategies for modern rechargeable batteries. *Accounts of Chemical Research*, 46(5):1053–1061, 2013. PMID: 22746097.

[11] H. Zabel and S. A. Solin. Graphite intercalation compounds i. *Springer Series in Materials Science*, 1990.

[12] M. Stanley Whittingham. *Intercalation Chemistry*, chapter 1: Intercalation chemistry: An Introduction. Academic Press Inc. New York, 1982.

[13] A. N. Dey. Electrochemical alloying of lithium in organic electrolytes. *Journal of the Electrochemical Society*, 118:1547, 1971.

[14] Sujong Chae, Minseong Ko, Kyungho Kim, Kihong Ahn, and Jaephil Cho. Confronting issues of the practical implementation of si anode in high-energy lithium-ion batteries. *Joule*, 1(1):47–60, 2017.

[15] Dominique Larcher, Shane Beattie, Mathieu Morcrette, Kristina Edström, Jean-Claude Jumas, and Jean-Marie Tarascon. Recent findings and prospects in the field of pure metals as negative electrodes for li-ion batteries. *J. Mater. Chem.*, 17:3759–3772, 2007.

[16] Gaojie Li, Siguang Guo, Ben Xiang, Shixiong Mei, Yang Zheng, Xuming Zhang, Biao Gao, Paul Chu, and Kaifu Huo. Recent advances and perspectives of microsized alloying-type porous anode materials in high-performance li- and na-ion batteries. *Energy Materials*, 2:200020, 06 2022.

[17] M. N. Obrovac and Leif Christensen. Structural changes in silicon anodes during lithium insertion/extraction. *Electrochemical and Solid-State Letters*, 7(5), January 2004.

[18] European Chemical Society. Element scarcity – euchems periodic table, 2023. Online; 10-08-2024.

[19] P. Poizot, S. Laruelle, S. Grugeon, L. Dupont, and J. Tarascon. Nano-sized transition-metal oxides as negative-electrode materials for lithium-ion batteries. *Nature*, 407:496–499, 2000.

[20] Seung-Ho Yu, Xinran Feng, Na Zhang, Jeesoo Seok, and Héctor D. Abruña. Understanding conversion-type electrodes for lithium rechargeable batteries. *Accounts of Chemical Research*, 51(2):273–281, 2018. PMID: 29373023.

[21] Xiujuan Wei, Xuanpeng Wang, Xin Tan, Qinyou An, and Liqiang Mai. Nanostructured conversion-type negative electrode materials for low-cost and high-performance sodium-ion batteries. *Advanced Functional Materials*, 28(46):1804458, 2018.

[22] Claude Delmas, Jean-Jacques Braconnier, Claude Fouassier, and Paul Hagenmuller. Electrochemical intercalation of sodium in naxcoo2 bronzes. *Solid State Ionics*, 3-4:165–169, 1981.

[23] S. Guo, Y. Sun, J. Yi, K. Zhu, Y. Zhu, G. Zhu, M. Chen, M. Ishida, and H. Zhou. Understanding sodium-ion diffusion in layered p2 and p3 oxides via experiments and first-principles calculations: a bridge between crystal structure and electrochemical performance. *NPG Asia Materials*, 8:e266–e266, 2016.

[24] S. Wang, C. Sun, N. Wang, and Q. Zhang. Ni- and/or mn-based layered transition metal oxides as cathode materials for sodium ion batteries: status, challenges and countermeasures. *Journal of Materials Chemistry A*, 7:10138–10158, 2019.

[25] Claude Delmas, Dany Carlier, and Marie Guignard. The layered oxides in lithium and sodium-ion batteries: A solid-state chemistry approach. *Advanced Energy Materials*, 11(2):2001201, 2021.

[26] A. Choi, J. Lim, H. Kim, S. C. Jung, H. Lim, H. Kim, M. Kwon, Y. K. Han, S. M. Oh, and K. Lee. Site-selective in situ electrochemical doping for mn-rich layered oxide cathode materials in lithium-ion batteries. *Advanced Energy Materials*, 8, 2017.

[27] Haowei Tang, Liping Duan, Jiaying Liao, Xinru Sheng, Jianzhi Xu, and Xiaosi Zhou. Magnesium ion-doped layered oxide cathodes for alkali-metal ion batteries: Recent research progress and outlook. *Energy Storage Materials*, 62:102935, 2023.

[28] J.B. Goodenough, H.Y-P. Hong, and J.A. Kafalas. Fast na+-ion transport in skeleton structures. *Materials Research Bulletin*, 11(2):203–220, 1976.

[29] H.Y-P. Hong. Crystal structures and crystal chemistry in the system na1+xzr2sixp3-xo12. *Materials Research Bulletin*, 11(2):173–182, 1976.

[30] Christian Masquelier and Laurence Croguennec. Polyanionic (phosphates, silicates, sulfates) frameworks as electrode materials for rechargeable li (or na) batteries. *Chemical Reviews*, 113(8):6552–6591, 2013. PMID: 23742145.

[31] Xin Wang, Shuai Tang, Wei Guo, Yongzhu Fu, and Arumugam Manthiram. Advances in multimetallic alloy-based anodes for alkali-ion and alkali-metal batteries. *Materials Today*, 50:259–275, 2021.

[32] Libin Fang, Naoufal Bahlawane, Wenping Sun, Hongge Pan, Ben Bin Xu, Mi Yan, and Yinzhu Jiang. Conversion-alloying anode materials for sodium ion batteries. *Small*, 17(37), July 2021.

[33] Sumair Imtiaz, Ibrahim Saana Amiinu, Yang Xu, Tadhg Kennedy, Chris Blackman, and Kevin M. Ryan. Progress and perspectives on alloying-type anode materials for advanced potassium-ion batteries. *Materials Today*, 48:241–269, 2021.

[34] Qichao Wu, Rongli Jiang, Lixue Mu, and Senyuan Xu. Fe3o4 anodes for lithium batteries: Production techniques and general applications. *Comptes Rendus Chimie*, 22(1):96–102, 2019.

[35] Taehoon Kim, Wentao Song, Dae-Yong Son, Luis K. Ono, and Yabing Qi. Lithium-ion batteries: outlook on present, future, and hybridized technologies. *J. Mater. Chem. A*, 7:2942–2964, 2019.

[36] Aurélien Etiemble, Nicolas Besnard, Anne Bonnin, Jérôme Adrien, Thierry Douillard, Pierre Tran-Van, L. Gautier, J. Badot, Eric Maire, and Bernard Lestriez. Multiscale morphological characterization of process induced heterogeneities in blended positive electrodes for lithium–ion batteries. *Journal of Materials Science*, 52, 04 2017.

[37] Xiulin Fan, Chao Luo, Julia Lamb, Yujie Zhu, Kang Xu, and Chunsheng Wang. Pedot encapsulated feof nanorod cathodes for high energy lithium-ion batteries. *Nano Letters*, 15(11):7650–7656, 2015. PMID: 26451460.

[38] Hao Zhang, Yang Yang, Dongsheng Ren, Li Wang, and Xiangming He. Graphite as anode materials: Fundamental mechanism, recent progress and advances. *Energy Storage Materials*, 36:147–170, 2021.

[39] Atsushi Funabiki, Minoru Inaba, Takeshi Abe, and Zempachi Ogumi. Stage transformation of lithium-graphite intercalation compounds caused by electrochemical lithium intercalation. *Journal of The Electrochemical Society*, 146(7):2443, 1999.

[40] IA Udod. Sodium-graphite intercalation compound of the first stage: two-dimensional structure and stability. *Synthetic Metals*, 88(2):127–131, 1997.

[41] R. Asher and S. A. Wilson. Lamellar compound of sodium with graphite. *Nature*, 181:409–410, 1958.

[42] K. S. Novoselov, A. K. Geim, S. V. Morozov, D. Jiang, Y. Zhang, S. V. Dubonos, I. V. Grigorieva, and A. A. Firsov. Electric field effect in atomically thin carbon films. *Science*, 306(5696):666–669, 2004.

[43] Dale A. C. Brownson, Graham C. Smith, and Craig E. Banks. Graphene oxide electrochemistry: the electrochemistry of graphene oxide modified electrodes reveals coverage dependent beneficial electrocatalysis. *Royal Society Open Science*, 4(11):171128, 2017.

[44] Y. Tian, Z. Yu, L. Cao, X. L. Zhang, C. Sun, and D. Wang. Graphene oxide: an emerging electromaterial for energy storage and conversion. *Journal of Energy Chemistry*, 55:323–344, 2021.

[45] Thomas M. McCoy, Geosmin Turpin, Boon Mian Teo, and Rico F. Tabor. Graphene oxide: a surfactant or particle? *Current Opinion in Colloid & Interface Science*,

39:98–109, 2019. Special Topic Section: Outstanding Young Researchers in Colloid and Interface Science.

[46] Rajesh Kumar, Sumanta Sahoo, Ednan Joanni, Rajesh K. Singh, Keiichiro Maegawa, Wai Kian Tan, Go Kawamura, Kamal K. Kar, and Atsunori Matsuda. Heteroatom doped graphene engineering for energy storage and conversion. *Materials Today*, 39:47–65, 2020.

[47] X. Wang, G. Sun, P. Routh, D. H. Kim, W. Huang, and P. Chen. Heteroatom-doped graphene materials: syntheses, properties and applications. *Chem. Soc. Rev.*, 43:7067–7098, 2014.

[48] S. Yadav and A. Devi. Recent advancements of metal oxides/nitrogen-doped graphene nanocomposites for supercapacitor electrode materials. *Journal of Energy Storage*, 30:101486, 2020.

[49] Haibo Wang, Thandavarayan Maiyalagan, and Xin Wang. Review on recent progress in nitrogen-doped graphene: Synthesis, characterization, and its potential applications. *ACS Catalysis*, 2(5):781–794, 2012.

[50] Hyun-Jung Choi, Sun-Min Jung, Jeong-Min Seo, Dong Wook Chang, Liming Dai, and Jong-Beom Baek. Graphene for energy conversion and storage in fuel cells and supercapacitors. *Nano Energy*, 1(4):534–551, 2012.

[51] Anastasios Stergiou, Rubén Cantón-Vitoria, Maria N. Psarrou, Solon P. Economopoulos, and Nikos Tagmatarchis. Functionalized graphene and targeted applications – highlighting the road from chemistry to applications. *Progress in Materials Science*, 114:100683, 2020.

[52] Aristides Bakandritsos, Petr Jakubec, Martin Pykal, and Michal Otyepka. Covalently functionalized graphene as a supercapacitor electrode material. *FlatChem*, 13:25–33, 2019.

[53] Ruiying Shi, Cuiping Han, Huan Duan, Lei Xu, Dong Zhou, Hongfei Li, Junqin Li, Feiyu Kang, Baohua Li, and Guoxiu Wang. Redox-active organic sodium anthraquinone-2-sulfonate (aqs) anchored on reduced graphene oxide for high-performance supercapacitors. *Advanced Energy Materials*, 8(31), September 2018.

[54] Jingjing Xu, Kai Wang, Sheng-Zhen Zu, Bao-Hang Han, and Zhixiang Wei. Hierarchical nanocomposites of polyaniline nanowire arrays on graphene oxide sheets with synergistic effect for energy storage. *ACS Nano*, 4(9):5019–5026, 2010.

[55] Jörg Neugebauer and T. Hickel. Density functional theory in materials science. *Wiley interdisciplinary reviews. Computational molecular science*, 3:438–448, 09 2013.

[56] A. Szabo and N. S. Ostlund. *Modern quantum chemistry: Introduction to advanced electronic structure theory.* McGraw-Hill, 1989.

[57] T. J. Zielinski, E. Harvey, R. J. Sweeney, and D. M. Hanson. Quantum states of atoms and molecules. *Journal of Chemical Education*, 82:1880, 2005.

[58] Hossein Hajiabadi. Hartree fock method: A simple explanation, 2022. Online; 31-07-2025.

[59] P. Hohenberg and W. Kohn. Inhomogeneous electron gas. *Phys. Rev.*, 136:B864–B871, Nov 1964.

[60] Ann Mattsson and Kevin Leung. Designing meaningful density functional theory calculations in materials science—a primer. *Modelling Simul. Mater. Sci. Eng.*, 13, 01 2005.

[61] A. H. Larsen and J. J. Mortensen. The atomic simulation environment—a python library for working with atoms. *Journal of Physics: Condensed Matter*, 29:273002, 2017.

[62] NIH3D. Aniline (version 2) [3d model], 2023. Online; 29-07-2025.

[63] NIH3D. Phenol (version 2) [3d model], 2023. Online; 29-07-2025.

[64] Koichi Momma and Fujio Izumi. *VESTA3* for three-dimensional visualization of crystal, volumetric and morphology data. *Journal of Applied Crystallography*, 44(6):1272–1276, Dec 2011.

[65] R. D. Shannon. Revised effective ionic radii and systematic studies of interatomic distances in halides and chalcogenides. *Acta Crystallographica Section A*, 32(5):751–767, 1976.

[66] J. Hafner and G. Kresse. *The Vienna AB-Initio Simulation Program VASP: An Efficient and Versatile Tool for Studying the Structural, Dynamic, and Electronic Properties of Materials*, pages 69–82. Springer US, Boston, MA, 1997.

[67] VASP team. Encut, 2024. Online; 30-07-2025.

[68] VASP team. Prec, 2024. Online; 30-07-2025.

[69] VASP team. Ediff, 2025. Online; 30-07-2025.

[70] VASP team. Algo, 2025. Online; 30-07-2025.

[71] VASP team. Isif, 2024. Online; 30-07-2025.

[72] VASP team. Nsw, 2024. Online; 30-07-2025.

[73] VASP team. Ibrion, 2025. Online; 30-07-2025.

[74] VASP team. Ediffg, 2022. Online; 30-07-2025.

[75] VASP team. Ivdw, 2025. Online; 30-07-2025.

[76] VASP team. ismear, 2025. Online; 30-07-2025.

[77] VASP team. Poscar, 2025. Online; 30-07-2025.

[78] VASP team. Poscar, 2024. Online; 30-07-2025.

[79] VASP team. Kpoints, 2024. Online; 30-07-2025.

[80] DB infotech. How to perform bader charge calculation in vasp and analysis, 2023. Online; 30-07-2025.

[81] Nabil Khossossi. Energies for H_2 and bulk sodium calculated using DFT-D3.

[82] Shuhan Zhao, Zhongyang Luo, Mengxiang Fang, Qinhui Wang, and Jianmeng Cen. Molecular simulation of graphene growth reactions at various temperatures derived from benzene in coal tar aromatic hydrocarbons. *Energies*, 18(2), 2025.

[83] James Ashenhurst. Activating and deactivating groups in electrophilic aromatic substitution, 2025. Online; 3-08-2025.

[84] William E. Gent, Iwnetim Iwnetu Abate, Wanli Yang, Linda F. Nazar, and William C. Chueh. Design rules for high-valent redox in intercalation electrodes. *Joule*, 4(7):1369–1397, 2020.

[85] James Ashenhurst. In summary: Free radicals, 2022. Online; 3-08-2025.

[86] Ian Hunt. Substituent effects (contd.), n.d. Online; 23-07-2025.

[87] Fatima, Yangchao Liao, Sara A. Tolba, Luis Alberto Ruiz Pestana, and Wenjie Xia. Chapter one - electronic structure and density functional theory. In Wenjie Xia and Luis Alberto Ruiz Pestana, editors, *Fundamentals of Multiscale Modeling of Structural Materials*, pages 3–35. Elsevier, 2023.

[88] NIST. Jarvis-dft, 2025. Online; 3-08-2025.

A Convergence Tests

ENCUT (eV)	Total Free Energy (eV)	Energy/Atom (eV)
200	-251,044	-7,384
225	-253,381	-7,452
250	-256,829	-7,554
275	-258,027	-7,589
300	-258,891	-7,614
325	-258,866	-7,614
350	-258,659	-7,608
375	-258,541	-7,604
400	-258,467	-7,602
425	-258,370	-7,599
450	-258,334	-7,598
475	-258,318	-7,598
500	-258,285	-7,597
525	-258,294	-7,597
550	-258,306	-7,597
575	-258,328	-7,598
600	-258,356	-7,599
625	-258,387	-7,600
650	-258,420	-7,601
675	-258,451	-7,602
700	-258,476	-7,602
725	-258,493	-7,603
750	-258,507	-7,603
775	-258,531	-7,604
800	-258,537	-7,604
825	-258,534	-7,604
850	-258,542	-7,604
875	-258,544	-7,604
900	-258,545	-7,604
925	-258,552	-7,604
950	-258,554	-7,605
975	-258,555	-7,605
1000	-258,557	-7,605

Table 11: Convergence test of ENCUT values between 200 eV and 1000 eV for ever 25 eV, their corresponding total free energy, and energy per atom. The converged system was a 3x3 graphene layer with a $NHCH_3$-benzene spacer. The systems consists of 34 atoms.

EDIFF (eV)	Total Free Energy (eV)	Energy/Atom (eV)
1	-258,369	-7,599
1E-01	-258,324	-7,598
1E-02	-258,315	-7,597
1E-03	-258,312	-7,597
1E-04	-258,319	-7,598
1E-05	-258,319	-7,598
1E-06	-258,319	-7,598
1E-07	-258,319	-7,598
1E-08	-258,319	-7,598
1E-09	-258,319	-7,598
1E-10	-258,319	-7,598

Table 12: Convergence test of EDIFF values between 1 eV and 10^{-10} eV, their corresponding total free energy, and energy per atom. The converged system was a 3x3 graphene layer with a $NHCH_3$-benzene spacer. The systems consists of 34 atoms.

SIGMA (eV)	Total Free Energy (eV)	Energy/Atom (eV)
2	-261,270	-7,684
2E-01	-258,356	-7,599
2E-02	-258,319	-7,598
2E-03	-258,317	-7,598
2E-04	-258,317	-7,598
2E-05	-258,317	-7,598
2E-06	-257,267	-7,567
2E-07	-257,267	-7,567
2E-08	-257,267	-7,567
2E-09	-257,267	-7,567

Table 13: Convergence test of SIGMA values between 2 eV and $2 * 10^{-9}$ eV, their corresponding total free energy, and energy per atom. The converged system was a 3x3 graphene layer with a $NHCH_3$-benzene spacer. The systems consists of 34 atoms.

KPOINTS	Total Free Energy (eV)	Energy/Atom (eV)
1	-254,490	-7,485
2	-258,059	-7,590
3	-258,292	-7,597
4	-258,305	-7,597
5	-258,289	-7,597
6	-258,299	-7,597
7	-258,283	-7,597
8	-258,289	-7,597
9	-258,284	-7,597
10	-258,286	-7,597
11	-258,286	-7,597
12	-258,287	-7,597
13	-258,288	-7,597
14	-258,287	-7,597
15	-258,288	-7,597
16	-258,287	-7,597
17	-258,288	-7,597
18	-258,287	-7,597
19	-258,287	-7,597
20	-258,287	-7,597

Table 14: Convergence test of KPOINTS with 1 to 20 **k**-points, their corresponding total free energy, and energy per atom. The converged system was a 3x3 graphene layer with a $NHCH_3$-benzene spacer. The systems consists of 34 atoms.

total vaccuum z direction (Å)	Total Free Energy (eV)	Energy/Atom (eV)
10	-258,556	-7,605
11	-258,456	-7,602
12	-258,384	-7,600
13	-258,347	-7,598
14	-258,336	-7,598
15	-258,327	-7,598
16	-258,317	-7,598
17	-258,311	-7,597
18	-258,312	-7,597
19	-258,304	-7,597
20	-258,305	-7,597
21	-258,301	-7,597
22	-258,299	-7,597
23	-258,295	-7,597
24	-258,294	-7,597
25	-258,298	-7,597
26	-258,295	-7,597
27	-258,293	-7,597
28	-258,294	-7,597
29	-258,294	-7,597
30	-258,295	-7,597
31	-258,292	-7,597
32	-258,291	-7,597
33	-258,290	-7,597
34	-258,290	-7,597
35	-258,293	-7,597
36	-258,288	-7,597
37	-258,288	-7,597
38	-258,288	-7,597
39	-258,289	-7,597
40	-258,292	-7,597
41	-258,284	-7,597
42	-258,289	-7,597
43	-258,287	-7,597
44	-258,287	-7,597
45	-258,290	-7,597
46	-258,283	-7,597
47	-258,287	-7,597
48	-258,286	-7,597
49	-258,287	-7,597
50	-258,289	-7,597

Table 15: Convergence test of total vacuum height from 10 Å to 50 Å, their corresponding total free energy, and energy per atom. The converged system was a 3x3 graphene layer with a $NHCH_3$-benzene spacer. The systems consists of 34 atoms.

B Speed Test

ntasks	CPU /Task	NCORE	KPAR	It.	Time (min)	Time/It (min)	CPU Efficiency (%)
2	48	8	2	20	180	9	2.08
2	48	16	2	20	180	9	2.08
8	12	8	2	26	63.51	2.44	8.29
16	6	8	2	26	49.10	1.89	16.58
16	6	16	2	26	29.35	1.13	16.57
16	6	32	2	26	30.29	1.17	16.25
32	3	32	2	26	13.36	0.52	32.96
144	1	32	2	27	4.99	0.18	95.2
96	1	32	2	26	7.18	0.28	97.28
144	1	32	3	26	5.37	0.21	95.53
144	1	64	3	26	7.06	0.27	96.81
144	1	64	2	26	5.65	0.22	95.97

Table 16: Testing the effect different NCORE and KPAR values, in combination with ntask and cpu/task input for the DelftBlue supercomputer. The test was run on a static energy calculation with NSW=0, for a 6x6 graphene layer with a $NHCH_3$-benzene spacer attached.

C POSCAR

```
 C  H  N Na
   1.00000000000000
    14.8128967285000002    0.0000000000000000    0.0000000000000000
    -7.4064449478999999   12.8283468430000003    0.0000000000000000
     0.0000000000000000    0.0000000000000000   30.0000000000000000
   C    H    N    Na
    79     8     1     2
Selective dynamics
Direct
  0.0527668968092172  0.0258637741137377  0.3532038330999967   F   F   F
  0.1083178892664662  0.1369969397856607  0.3530199825666642   F   F   F
  0.0526974499075550  0.1925043314795900  0.3525050878666676   F   F   F
  0.1080954969210524  0.3034750521361502  0.3529127836333359   F   F   F
  0.0527206398530424  0.3590752184497958  0.3522354960333303   F   F   F
  0.1083668246728706  0.4702193736905045  0.3527573347000015   F   F   F
  0.0528072863927420  0.5258082747178463  0.3526402414000032   F   F   F
  0.1083544120222655  0.6368534564886659  0.3532856404666660   F   F   F
  0.0526771620050681  0.6924275160089692  0.3538124263333344   F   F   F
  0.1083894521257633  0.8036231994791549  0.3539356589333309   F   F   F
  0.0526706986176748  0.8591079115555544  0.3541166186333342   F   F   F
  0.1083217784453154  0.9703639149570193  0.3535651266666662   F   F   F
  0.2195790857340825  0.0260904263890112  0.3534656464999983   F   F   F
  0.2749643922058738  0.1370884179795624  0.3539032935999984   F   F   F
  0.2194011956949282  0.1925608665116414  0.3537926376000016   F   F   F
  0.2747810780986271  0.3036833107709285  0.3550269603666649   F   F   F
  0.2192492634302994  0.3590445518327527  0.3544812798666683   F   F   F
  0.2748495042161636  0.4699358939838447  0.3553143143666659   F   F   F
  0.2194551080737952  0.5256986022076475  0.3540033399999984   F   F   F
  0.2749830186158277  0.6367303132637971  0.3544095754666685   F   F   F
  0.2196026444773622  0.6923603415701649  0.3536718487666661   F   F   F
  0.2750742733473217  0.8035855293096574  0.3535493910333329   F   F   F
  0.2195416241874142  0.8592107296361817  0.3535384237666648   F   F   F
  0.2750871777686399  0.9703716039446348  0.3532855808666682   F   F   F
  0.3862947523221507  0.0261072702584997  0.3525977134666647   F   F   F
  0.4418548643139246  0.1371420472591893  0.3526668846666681   F   F   F
  0.3865147530975790  0.1933371275624154  0.3543481230666643   F   F   F
  0.4415558576665504  0.3034685551961260  0.3568639457333305   F   F   F
  0.3858858049143876  0.3596607744915801  0.3582495451000014   F   F   F
  0.4394996464312797  0.4690076112404995  0.3627094030333353   F   F   F
  0.3859434127827868  0.5249471664133125  0.3588491082333363   F   F   F
  0.4415284097642456  0.6368680000617601  0.3581982254999971   F   F   F
  0.3865306377089368  0.6920057534805437  0.3554824888666701   F   F   F
  0.4418679476281042  0.8035801649395751  0.3538832664333356   F   F   F
  0.3862924277786846  0.8590472340567672  0.3531381487999994   F   F   F
  0.4418052136999222  0.9703289866061198  0.3522621989333317   F   F   F
  0.5528335571350880  0.0258516370861130  0.3515297472333359   F   F   F
  0.6083888411181135  0.1370422541981142  0.3509300350999993   F   F   F
  0.5528710484586412  0.1926836520131019  0.3515562712999980   F   F   F
  0.6085888147382192  0.3039134740987635  0.3522469699333328   F   F   F
  0.5535089373369502  0.3600229323016890  0.3559601604999969   F   F   F
  0.6093504428794319  0.4693205654386574  0.3608297109666694   F   F   F
  0.5532450080112525  0.5252303481080745  0.3768583834333299   F   F   F
  0.6093875765953527  0.6387206912378645  0.3626977801333311   F   F   F
```

```
0.5535749792977143  0.6923286318724919  0.3581290543000009   F   F   F
0.6086366772629788  0.8035520910962006  0.3544910251999980   F   F   F
0.5529110431483133  0.8590642213586150  0.3531690240000032   F   F   F
0.6084018349477631  0.9702212810679924  0.3518415689333310   F   F   F
0.7195409536439072  0.0258532836739604  0.3514934778333298   F   F   F
0.7750478982975437  0.1369582563912886  0.3508170246999995   F   F   F
0.7195223569832621  0.1925491392796133  0.3506078421999987   F   F   F
0.7750898003328430  0.3035598993119635  0.3509919345333330   F   F   F
0.7194969654043817  0.3592430353186700  0.3519905209666661   F   F   F
0.7749469280173926  0.4701424241028391  0.3536326587333321   F   F   F
0.7189468741470719  0.5251594781814077  0.3577229082666662   F   F   F
0.7753238678358017  0.6370291710236415  0.3589036464666648   F   F   F
0.7189908623881536  0.6925937533290281  0.3591721952000029   F   F   F
0.7749387622057498  0.8036841154342369  0.3554716408333363   F   F   F
0.7195318340916756  0.8591840862966933  0.3540931344000029   F   F   F
0.7751111388727523  0.9704345465053450  0.3524992764000032   F   F   F
0.8860994577113743  0.0258686393548118  0.3524231016666661   F   F   F
0.9416376948692005  0.1369589418264496  0.3518735170333329   F   F   F
0.8861066102661894  0.1924967765700458  0.3511864244999998   F   F   F
0.9416537881117506  0.3035794198318769  0.3513434827333342   F   F   F
0.8860954045975902  0.3591271042467881  0.3512936532333342   F   F   F
0.9416716098972202  0.4702704548631615  0.3521249294333302   F   F   F
0.8861305713402743  0.5258231163028455  0.3532256781999976   F   F   F
0.9416654706028140  0.6368399858519496  0.3544926643333355   F   F   F
0.8855184912527463  0.6921666860640840  0.3562676906666695   F   F   F
0.9416641593130848  0.8036795258327274  0.3551139831666674   F   F   F
0.8861162066496817  0.8591825366036403  0.3544839918666653   F   F   F
0.9416389465081636  0.9702759980949480  0.3532195687333299   F   F   F
0.5569607615371055  0.4413000941028571  0.4527221917999995   F   F   F
0.5481064915836455  0.4359163641612511  0.4990676939333341   F   F   F
0.5337409377198767  0.5077997446377580  0.5234663486333346   F   F   F
0.5279483198992736  0.5880631804180183  0.5008554458666694   F   F   F
0.5372077226570937  0.5932338833785593  0.4540064632999972   F   F   F
0.5508442521232126  0.5206972360312250  0.4297178685666694   F   F   F
0.5236608982317179  0.6738399863047704  0.5709958672666673   F   F   F
0.5690265893835971  0.3841220438850925  0.4351141452666667   F   F   F
0.5530028939041145  0.3740351200137866  0.5166702270666690   F   F   F
0.5275186300017296  0.5017776488879733  0.5596470236666633   F   F   F
0.5332498550530858  0.6561902761144438  0.4370094239666642   F   F   F
0.6006816029417053  0.6886299252830383  0.5827251076666684   F   F   F
0.4633770882853483  0.6044684052358065  0.5885317921666697   F   F   F
0.5142648815804023  0.7400461435278629  0.5806442498999971   F   F   F
0.5262752771674073  0.7241997123011501  0.5052770376333342   F   F   F
0.5115393996292497  0.6603019237527192  0.5231829285666691   F   F   F
0.3537844176287948  0.3856925734809877  0.4407739309272571   F   F   F
0.8230697816840028  0.4181875507609562  0.4284167445720183   T   T   T
```

D Adsorption Energies

1-Layer Structure			*2-layer structure*		
Number of Ions	**Total Free Energy (eV)**	**Adsorption Energy (eV)**	**Number of Ions**	**Total Free Energy (eV)**	**Adsorption Energy (eV)**
0	-670.460		0	-1343.997	
6	-677.220	-0.907	6	-1344.261	0.176
12	-684.307	-0.934			

Table 17: Calculated total and adsorption energies of 6 and 12 inserted ions for 1-layer graphene, and 6 ions for the 2-layer graphene.

1-Layer Structure			*2-layer structure*		
Number of Ions	**Total Free Energy (eV)**	**Adsorption Energy (eV)**	**Number of Ions**	**Total Free Energy (eV)**	**Adsorption Energy (eV)**
0	-762.381		0	-1440.878	
1	-772.089	-9.488	1	-1442.115	-1.017
2	-772.261	-4.720	2	-1443.254	-0.968
3	-773.810	-3.590	3	-1444.860	-1.107
4	-775.154	-2.973	4	-1446.434	-1.169
5	-776.052	-2.514	5	-1447.128	-1.030
6	-777.178	-2.246	6	-1448.150	-0.992
7	-778.316	-2.056	7	-1449.822	-1.058
8	-779.448	-1.913	8	-1450.874	-1.029
9	-780.516	-1.795	9	-1452.369	-1.057
10	-781.612	-1.703	10	-1453.344	-1.027
11	-782.094	-1.572	11	-1454.435	-1.013
12	-783.713	-1.558	12	-1455.488	-0.998
13	-784.872	-1.510	13	-1456.867	-1.010
14	-786.166	-1.479	14	-1458.419	-1.033
15	-787.744	-1.471	15	-1459.844	-1.044
16	-789.057	-1.447	16	-1461.135	-1.046
17	-790.424	-1.430	17	-1462.433	-1.048
18	-791.892	-1.420	18	-1464.047	-1.067

Table 18: Calculated total adsorption energies of the step-by-step inserted sodium from 1 to 18 ions into the meta-$NHCH_3$ for the 1 and 2-layer configuration.

1-Layer Structure			*2-layer structure*		
Number of Ions	**Total Free Energy (eV)**	**Adsorption Energy (eV)**	**Number of Ions**	**Total Free Energy (eV)**	**Adsorption Energy (eV)**
0	-762.399		0	-1440.822	
1	-772.038	-9.419	1	-1442.913	-1.871
2	-772.974	-5.067	2	-1444.377	-1.558
3	-773.780	-3.573	3	-1445.065	-1.194
4	-774.967	-2.922	4	-1446.742	-1.260
5	-776.089	-2.518	5	-1447.579	-1.131
6	-777.145	-2.238	6	-1449.231	-1.181
12	-785.006	-1.664	12	-1457.102	-1.137

Table 19: Calculated total and adsorption energies of the step-by-step inserted sodium for 1 to 6 and 12 ions inserted into the para-$NHCH_3$ for the 1 and 2-layer configuration.

1-Layer Structure			*2-layer structure*		
Number of Ions	**Total Free Energy (eV)**	**Adsorption Energy (eV)**	**Number of Ions**	**Total Free Energy (eV)**	**Adsorption Energy (eV)**
0	-761.491		0	-1439.912	
1	-771.682	-9.971	1	-1442.440	-2.309
2	-772.409	-5.239	2	-1443.482	-1.565
3	-774.075	-3.975	3	-1445.289	-1.573
4	-775.062	-3.173	4	-1446.102	-1.328
5	-776.197	-2.721	5	-1447.505	-1.299
6	-777.232	-2.404	6	-1448.591	-1.227
12	-784.752	-1.718	12	-1456.968	-1.201

Table 20: Calculated total and adsorption energies of the step-by-step inserted sodium for 1 to 6 and 12 ions inserted into the ortho-$NHCH_3$ for the 1 and 2-layer configuration.

Number of Ions	Total Free Energy (eV)	Adsorption Energy (eV)
0	-1417.809	
1	-1420.176	-2.147
2	-1422.215	-1.983
3	-1423.109	-1.547
4	-1424.191	-1.376
5	-1425.593	-1.337
6	-1426.481	-1.225
12	-1434.558	-1.176
18	-1443.009	-1.180

Table 21: Calculated total and adsorption energies of the step-by-step inserted sodium for 1 to 6, 12 and 18 ions inserted into the para-OH for the 1 and 2-layer configuration.

Number of Ions	Total Free Energy (eV)	Adsorption Energy (eV)
0	-1424.435	
1	-1426.489	-1.834
2	-1428.871	-1.999
3	-1430.115	-1.673
4	-1430.115	-1.200
5	-1431.012	-1.096
6	-1432.568	-1.136
12	-1440.814	-1.145
18	did not converge	

Table 22: Calculated total and adsorption energies of the step-by-step inserted sodium for 1 to 6, 12 and 18 ions inserted into the para-$NH2$ for the 1 and 2-layer configuration.

E 3D models

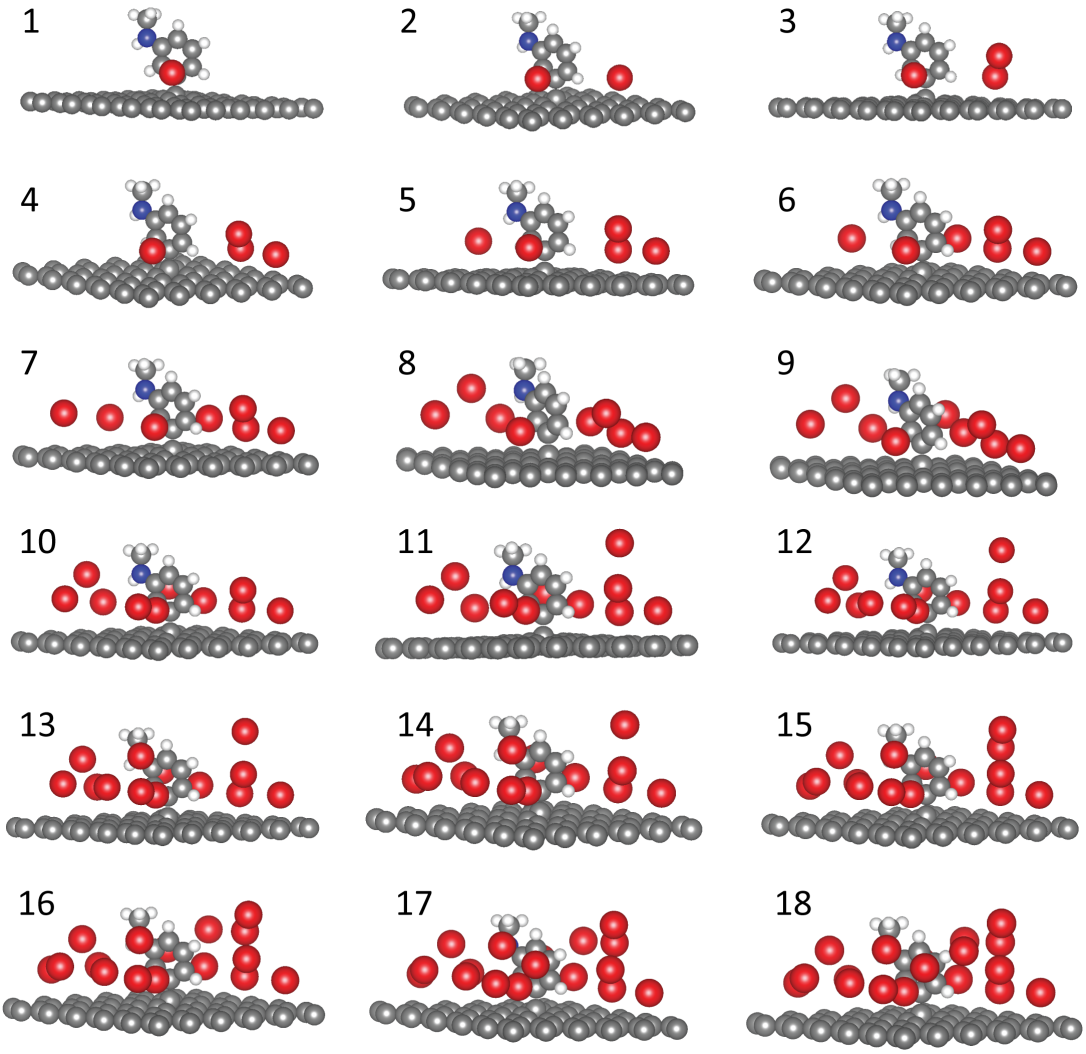

Fig. 29: 3D-model for every inserted atom from 1 to 18 in single-layer meta-$NHCH_3$. Grey is carbon, white is hydrogen, blue is nitrogen and red is sodium.

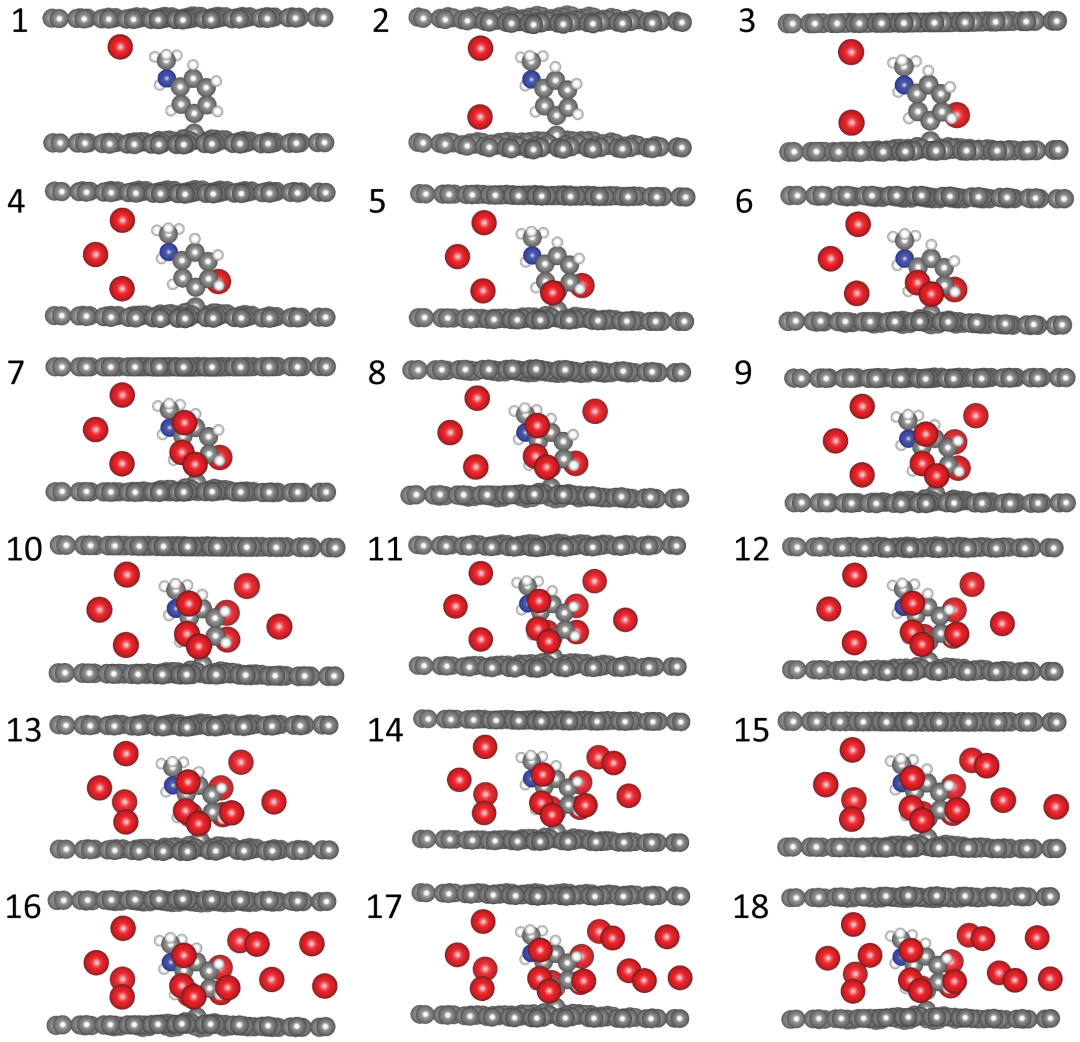

Fig. 30: 3D-model for every inserted atom from 1 to 18 in double-layer meta-$NHCH_3$. Grey is carbon, white is hydrogen, blue is nitrogen and red is sodium.

F Bader Charges

Na		*Spacer*		*Graphene*	
Average Bader Charge	**Corrected Bader Charge**	**Average Bader Charge**	**Corrected Bader Charge**	**Average Bader Charge**	**Corrected Bader Charge**
0.955	-0.045	2.612	0.050	4.012	0.012
0.992	-0.008	2.561	-0.002	4.023	0.023
0.980	-0.020	2.587	0.025	4.018	0.018
0.972	-0.028	2.543	-0.020	4.027	0.027
0.978	-0.022	2.531	-0.032	4.030	0.030
0.975	-0.025	2.517	-0.045	4.033	0.033
0.977	-0.023	2.569	0.007	4.036	0.036
0.856	-0.144	2.123	-0.439	4.034	0.034
1.634	0.634	2.182	-0.380	4.035	0.035
1.472	0.472	2.175	-0.388	4.036	0.036
1.439	0.439	2.129	-0.434	4.037	0.037
1.442	0.442	2.198	-0.364	4.038	0.038
1.362	0.362	2.233	-0.330	4.039	0.039
1.260	0.260	2.279	-0.283	4.044	0.044
1.226	0.226	2.267	-0.295	4.043	0.043
1.166	0.166	2.194	-0.369	4.043	0.043
1.214	0.214	2.286	-0.276	4.043	0.043
1.147	0.147	2.354	-0.209	4.042	0.042

Table 23: Bader Charges and corrected Bader charges of the single-layer meta-$NHCH_3$ structure. Corrected charges were calculated by subtracting the average valence charge.

Na		*Spacer*		*Graphene*	
Average Bader Charge	**Corrected Bader Charge**	**Average Bader Charge**	**Corrected Bader Charge**	**Average Bader Charge**	**Corrected Bader Charge**
0.007	-0.993	2.567	0.004	4.006	0.006
0.163	-0.837	2.569	0.006	4.011	0.011
0.215	-0.785	2.575	0.013	4.015	0.015
0.457	-0.543	2.574	0.012	4.014	0.014
0.369	-0.631	2.576	0.013	4.020	0.020
0.450	-0.550	2.586	0.023	4.020	0.020
0.517	-0.483	2.583	0.021	4.021	0.021
0.554	-0.446	2.585	0.023	4.022	0.022
0.608	-0.392	2.585	0.022	4.022	0.022
0.630	-0.370	2.586	0.024	4.023	0.023
0.626	-0.374	2.588	0.026	4.026	0.026
0.623	-0.377	2.595	0.033	4.028	0.028
0.648	-0.352	2.597	0.035	4.028	0.028
0.655	-0.345	2.597	0.035	4.030	0.030
0.672	-0.328	2.597	0.035	4.030	0.030
0.674	-0.326	2.597	0.035	4.032	0.032
0.683	-0.317	2.598	0.035	4.034	0.034
0.708	-0.292	2.597	0.035	4.033	0.033

Table 24: Bader Charges and corrected Bader charges of the double-layer meta-$NHCH_3$ structure. Corrected charges were calculated by subtracting the average valence charge.